

REVIEW

[View Article Online](#)
[View Journal](#) | [View Issue](#)



Cite this: *Chem. Sci.*, 2021, **12**, 6800

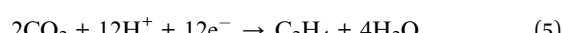
Received 9th March 2021
Accepted 7th April 2021

DOI: 10.1039/d1sc01375k
rsc.li/chemical-science

1. Introduction

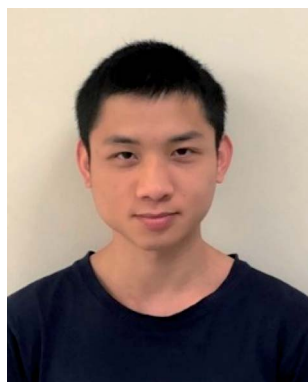
Excessive emission of CO_2 resulting from overconsumption of fossil fuels causes the green-house effect. The CO_2RR not only provides a solution to reduce CO_2 concentration in the atmosphere, but also is able to simultaneously produce valuable carbonaceous chemicals/fuels.^{1,2} Electrocatalytic reduction of CO_2 driven by renewable electricity is environmentally friendly, and has become a hotspot in the field of CO_2 conversion. The CO_2RR involves very complex reactions, coupled with multiple

proton and electron transfer steps,³ which can convert CO_2 into carbon monoxide (CO), methane (CH_4), formic acid (HCOOH), methanol (CH_3OH), ethylene (C_2H_4), ethanol ($\text{C}_2\text{H}_5\text{OH}$), etc:

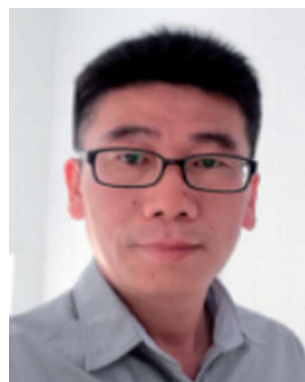


^aSchool of Chemical and Biomedical Engineering, Nanyang Technological University, 62 Nanyang Drive, Singapore, 637459, Singapore. E-mail: liubin@ntu.edu.sg

^bInstitute for Materials Science and Devices, Suzhou University of Science and Technology, Suzhou, 215009, China. E-mail: yanghb@mail.usts.edu.cn



Jincheng Zhang is currently a PhD student at Nanyang Technological University. His research interest focuses on coordination engineering of single-atom catalysts.



Hongbin Yang is a Professor at Suzhou University of Science and Technology. He received his B.S. (1998) from Lanzhou University and PhD (2008) from Fudan University. His active research interests include electrocatalysis, photoelectrochemistry and carbon-based catalysts.



CO	HCOOH			CH ₃ OH			CH ₄			C ₂₊			
Sc	Ti	V	Cr	Mn	Fe	Co	Ni	Cu	Zn	Ga	Ge	As	Se
Y	Zr	Nb	Mo	Tc	Ru	Rh	Pd	Ag	Cd	In	Sn	Sb	Te
La-Lu	Hf	Ta	W	Re	Os	Ir	Pt	Au	Hg	Tl	Pb	Bi	Po

Fig. 1 The reported elements in SACs for the electrochemical CO₂RR.

Many catalysts have been explored to break the robust C=O bond, such as sulfides,^{4–6} phosphides,^{7,8} oxides,^{9–13} and so on. However, the performance of the CO₂RR is still unsatisfactory, showing low activity and poor product selectivity,^{14,15} especially for liquid C₂₊ products. Therefore, developing highly active catalysts with good selectivity and stability is crucial for promoting this clean energy conversion technology.^{16–18}

Since Qiao *et al.*¹⁹ developed the Pt₁/FeO_x single atom catalyst (SAC) in 2011, SACs have received considerable attention. SACs usually consist of a metal center coordinated with non-metal atoms. Because most of the metal sites can be exposed at the catalyst's surface and they possess a unique electronic structure, SACs show high intrinsic catalytic activity.^{20–23} Additionally, SACs are ideal models for elucidating the structure–activity relationship because of their homogeneous atomically-dispersed active sites.^{24–27} Furthermore, coupled with *in situ* characterization techniques, the structural evolution of active sites in SACs can be probed, which helps to further design next-generation catalysts.^{28,29} Recently, the application of SACs achieved significant advancement in the field of electrochemical reactions.^{7,30} In the electrochemical CO₂RR, SACs exhibit encouraging performance in terms of catalytic activity, product selectivity, and stability.^{31–33} Fig. 1 summarizes the reported elements in SACs for the electrochemical CO₂RR.

The metal elements used to construct SACs for the electrochemical CO₂RR include three types, transition metal (Mo, Fe, Co, Ni, Cu, and Zn), noble metal (Pd, Ag and Ir) and p-block (Sn, Sb and Bi) elements (Fig. 1). Most of the reported SACs electrochemically reduce CO₂ to CO, especially TM-SACs. However,

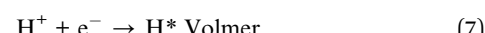
it is also reported that Co, Cu, Mo, Sn and Sb SACs can reduce CO₂ to liquid products (*e.g.*, HCOOH, CH₃OH, *etc.*). As shown in Fig. 1, for the same metal SAC, the reported major CO₂RR products are different, for example, Co-SAC can reduce CO₂ to CO or CH₃OH, and Sn and Sb-SAC can reduce CO₂ to CO or HCOOH. The determining factor for product selectivity is still under controversy. Therefore, to clearly elucidate the structure–activity relationship in the CO₂RR and further develop SACs with higher product selectivity, especially for C₂₊ products, a systematic review of previous studies of SACs in the CO₂RR is urgently needed. Fig. 2 shows the development of SAC-based electrocatalysts for the CO₂RR.

In this review, the strategies to enhance the CO₂RR performance are first outlined, including the suppression of the HER, and the generation of C₁ products and C₂₊ products. Then, recent advances in promoting CO₂RR performance using SACs are summarized. Finally, some challenges in this field are proposed and possible solutions are provided at the end.

2. Strategies to improve the CO₂RR

2.1. Suppression of the HER

The HER is the main side reaction competing with the CO₂RR. The HER can proceed *via* two mechanisms, the Volmer–Heyrovsky and the Volmer–Tafel mechanism.^{34–36} In the Volmer step, a proton from the electrolyte reacts with an electron to form an adsorbed hydrogen on the catalyst surface (H*). If the second step is the Heyrovsky reaction, the H* will directly react with a proton and another electron to generate H₂. If the Tafel reaction happens, another proton combines with another electron to form a second H*, which will couple with the first H* to generate H₂.

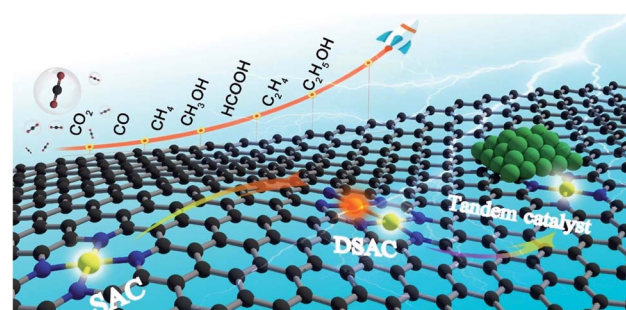


The Tafel route requires two adjacent active sites to adsorb two H*, which is difficult in the case of SACs. So, the Heyrovsky mechanism is more plausible for the HER on SACs. Previous studies have shown that the activation energy of the Heyrovsky

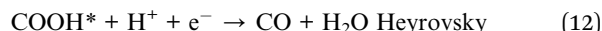


Bin Liu received his B.Eng. (1st Class Honors) and M.Eng. degrees in Chemical Engineering from the National University of Singapore and obtained his PhD degree in Chemical Engineering from the University of Minnesota in 2011. Thereafter, he moved to the University of California, Berkeley, and worked as a post-doctoral researcher in the Department of Chemistry from 2011 to 2012 before joining the School of Chemical and Biomedical Engineering at Nanyang Technological University as an Assistant Professor in 2012. He is now an Associate Professor at NTU. His main research interests are electrocatalysis, photovoltaics and photoelectrochemistry.

Open Access Article. Published on 26 Dzivanisiko 2021. Downloaded on 2026-02-13 22:27:07.
This article is licensed under a Creative Commons Attribution-NonCommercial 3.0 Unported Licence.

Fig. 2 The development of SAC-based electrocatalysts for the CO₂RR.

step is typically two times that of the Tafel step. Consequently, the HER can be considerably suppressed on SACs compared to their nanoparticle counterparts. A similar principle is also applicable to the CO_2 RR, where the Heyrovsky mechanism is more plausible.



The difference between the thermodynamic limiting potentials ($U_L(\text{CO}_2) - U_L(\text{H}_2)$) is a descriptor to indicate the selectivity of the CO_2 RR ($U_L(\text{CO}_2)$ and $U_L(\text{H}_2)$ are the thermodynamic limiting potentials for the CO_2 RR and HER, respectively). The larger the value, the higher the selectivity of CO.

The HER is the main side reaction competing with the CO_2 RR, which needs to be suppressed so as to improve the selectivity of the CO_2 RR. Jung *et al.* calculated the adsorption

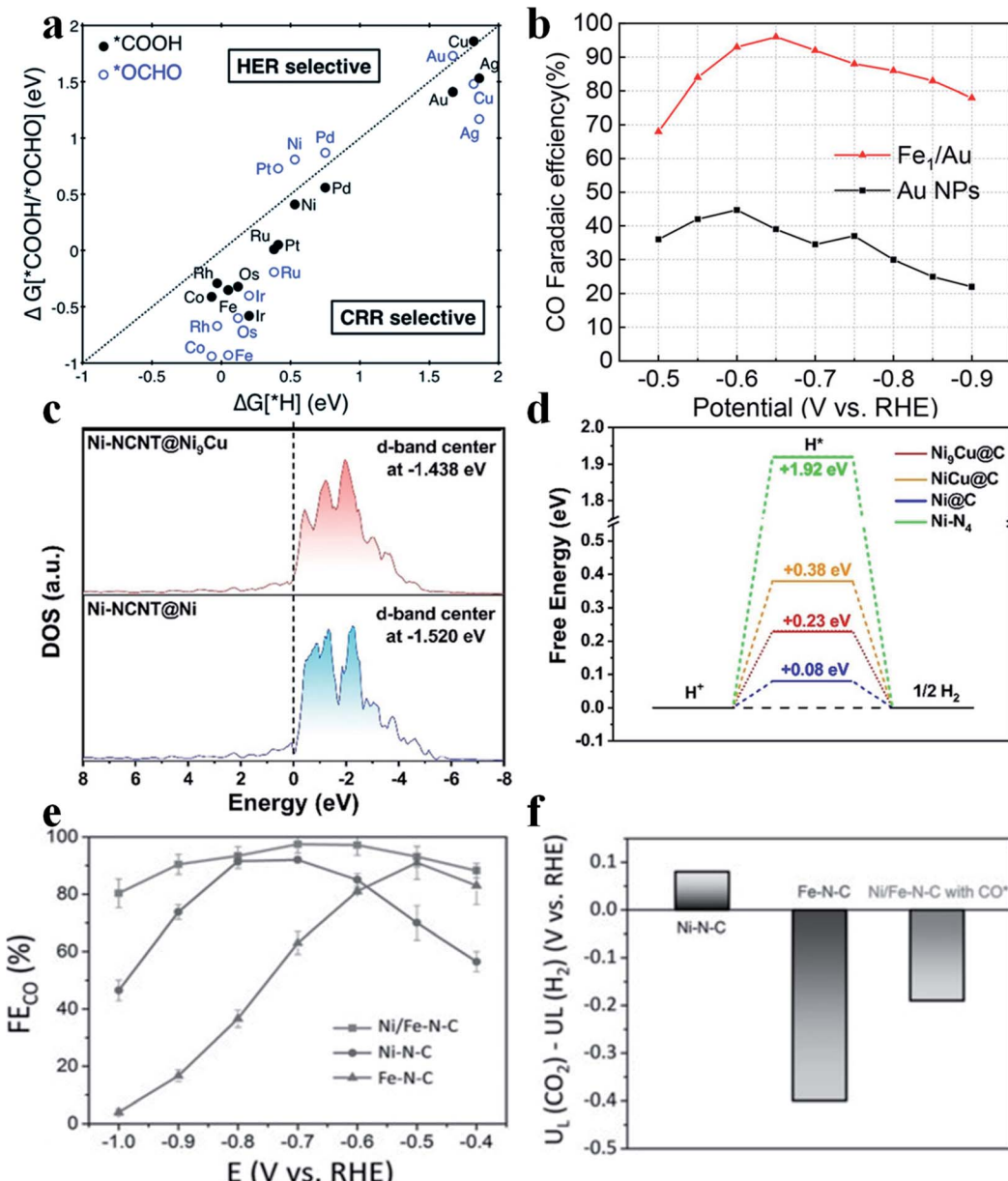


Fig. 3 (a) Free energy change of the first protonation step in the CO_2 RR and HER on various SACs. Catalysts below the dotted parity line are CO_2 RR selective. Reproduced with permission from ref. 7. Copyright (2017) The Royal Society of Chemistry. (b) CO faradaic efficiency of Fe_1/Au , compared with Au NPs, at different applied cathodic potentials. Reproduced with permission from ref. 37. Copyright (2020) American Chemical Society. (c) Calculated DOS for $\text{Ni}^1\text{-NCNT@Ni}$ and $\text{Ni}^1\text{-NCNT@Ni}_9\text{Cu}$. (d) The calculated free-energy diagram of the HER on the (111) surface of Ni@C , $\text{Ni}_9\text{Cu@C}$, NiCu@C , and Ni-N_4 sites. Reproduced with permission from ref. 38. Copyright (2020) Wiley-VCH. (e) FE_{CO} of Ni/Fe-N-C , Ni-N-C and Fe-N-C at various applied potentials. (f) Difference in limiting potentials for the CO_2 RR and HER for different catalysts. Reproduced with permission from ref. 39. Copyright (2019) Wiley-VCH.



energy of H ($\Delta G(H^*)$), *COOH and *OCHO ($\Delta G[*COOH/*OCHO]$) and found that most SACs possess a $\Delta G(H^*)$ larger than the $\Delta G[*COOH/*OCHO]$, suggesting that the CO₂RR was more favorable than the HER on most SACs (Fig. 3a).³⁷ Although the HER is intrinsically unfavorable on SACs, the selectivity towards CO₂RR products still needs to be further improved. Yao *et al.* reported that by introducing Fe atoms into Au nanoparticles (Au NPs), the HER could be effectively suppressed, which greatly enhanced the CO faradaic efficiency (FE) in the CO₂RR.³⁷ Furthermore, the introduced Fe atoms bound with O atoms in CO₂, while the nearby Au atoms bound with C atoms in CO₂. Such a synergistic effect boosted the performance of Fe/Au (Fig. 3b). Other metal elements have also been studied to constrain the HER in SACs. Liu *et al.* introduced Cu into Ni SAC to form Ni(i)-NCNT@Ni₉Cu to tune the adsorption energy of H*. Electrochemical results showed that Ni(i)-NCNT@Ni₉Cu delivered a specific current density of $-32.87 \text{ mA cm}^{-2}$ and a TOF of 1962 h^{-1} at an overpotential of 620 mV for generating CO with 97% FE_{CO}. DFT calculations found that the d-band center was upshifted from -1.520 eV to -1.438 eV after the introduction of Cu, which strengthened the adsorption of H* and thus further impeded the HER (Fig. 3c and d).³⁸ The HER dominates at high overpotentials in single Fe atom catalysts. Zhao *et al.* introduced single Ni atoms into Fe-SAC and found that such a dual atom center could efficiently regulate the adsorption energy of H*³⁹ to suppress the HER and thus promote FE_{CO} (Fig. 3e and f).

Another issue in the electrochemical CO₂RR is that the solubility of CO₂ in aqueous electrolyte is typically low (34 mM),⁴⁰ and the reactant diffusion limitation restricts the reaction rate of the CO₂RR particularly at high overpotentials, while the HER becomes more competitive. To tackle this challenge, many strategies have been developed, such as increasing the device pressure,⁴¹ lowering the reaction temperature,⁴² adopting a flow-cell device,⁴³ and using a solid electrolyte.⁴⁴

2.2. Generation of C₁ products

C_1 products from the CO_2RR include CO , HCOO^- , CH_3OH , and CH_4 . Fig. 4 lists the possible pathways for the C_1 products. To reduce CO_2 to CO , $^*\text{COOH}$ is first generated on the catalyst's surface *via* a proton coupled electron transfer (PCET) step, followed by $^*\text{CO}$ formation through dehydrogenation of $^*\text{COOH}$, which is finally desorbed from the catalyst to release CO .⁴⁵ If the catalyst adsorbs $^*\text{CO}$ very strongly, the catalytically active sites will be poisoned and the HER becomes dominant. If the catalyst adsorbs $^*\text{CO}$ loosely, $^*\text{CO}$ will be desorbed from the catalyst surface to generate CO . Only when the catalytic surface adsorbs $^*\text{CO}$ neither too strongly nor too weakly, further reduction reaction can take place. HCOO^- is formed *via* the $^*\text{OCHO}$ intermediate, which has a medium adsorption energy.⁴⁶ $^*\text{OCHO}$ can be bound to the catalyst surface *via* one or two oxygen atoms. As there are no neighbouring active sites, $^*\text{OCHO}$ is more likely to bind to the SAC *via* only one O atom as shown in Fig. 4. Both $^*\text{CHO}$ and $^*\text{COH}$ pathways are able to produce CH_4 , forming $^*\text{CHOH}$ and then $^*\text{CH}_2\text{OH}$ and finally branching into two routes (CH_3OH and CH_4).⁴⁷⁻⁵¹ $^*\text{C}$ is formed *via* dehydration of $^*\text{COH}$ and constitutes another pathway to generate CH_4 . Carbon deposition covered on the copper catalyst after the CO_2RR confirmed the existence of $^*\text{C}$. Furthermore, $^*\text{CH}_3\text{O}$ formed *via* protonation of $^*\text{CHO}$ is an important intermediate for CH_4 and CH_3OH .^{50,52-56} It is worth mentioning that the energy barriers for both pathways ($^*\text{CH}_2\text{OH}$ and $^*\text{CH}_3\text{O}$) to produce CH_3OH are high, making CH_3OH generation rather difficult.

2.3. Generation of C₂ products

C_2 products from the CO_2 RR include C_2H_4 , C_2H_5OH , C_2H_6 , CH_3COOH , $C_2H_6O_2$, *etc.* Several protonation and electron transfer steps engage in the formation of C_2 products, making the reactions very sophisticated. As many possible pathways are capable of generating the same product, this leads to controversy about the reaction mechanisms.

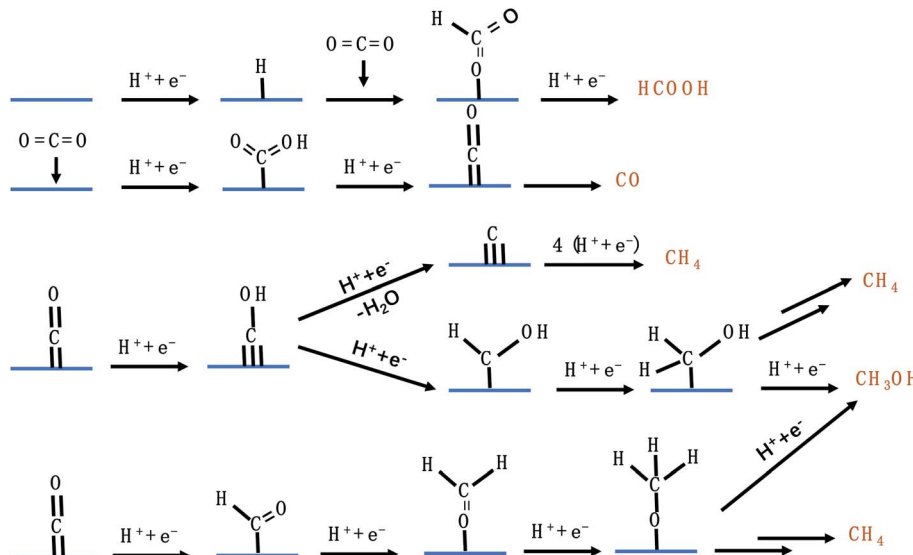


Fig. 4 The possible CO₂RR pathways for C₁ products.

Fig. 5 shows the possible CO₂RR pathways for C₂ products. In the first route, CH₂CHO* acts as an important intermediate to produce C₂H₄ and CH₃CH₂OH,⁵⁷ which can branch into two pathways. One transforms to *C₂H₄O, which dissociates and releases C₂H₄. The other forms CH₃CHO* which is further reduced to generate CH₃CH₂OH. It is noteworthy that the calculated energy barrier for CH₃CHO* → CH₃CH₂OH is 0.2 eV, which is higher than that for CH₂CHO* → *O + C₂H₄, explaining the higher selectivity for C₂H₄ than for CH₃CH₂OH among different C₂ products.^{58–62} In the second route, starting from *CO, CH₂OHCH₂OH can be formed through CO insertion into *CHO coupled with several protonation and electron transfer steps. *CHO can also undergo another pathway to produce CH₄. The pathway towards CH₄ production has a lower energy barrier than that towards CH₂OHCH₂OH production, disclosing that very little CH₂OHCH₂OH can be detected. In the third route, *CH₂, originating from *CO, serves as an important intermediate to produce CH₃COOH and C₂H₆.^{63–66} As discussed above, the C₂ pathways involve two close active sites to adsorb intermediates, which are severely limited in SACs. Consequently, very few groups have reported the generation of C₂ products on SACs *via* the CO₂RR.

3. SACs for the CO₂RR

3.1. Advantages of SACs

Compared with traditional catalysts, the metal single atom sites in SACs locate at the catalyst's surface. Such an attribute makes SACs possess maximum atom utilization efficiency and thus exhibit excellent catalytic performance. Furthermore, the metal centers in SACs can be influenced by the near-range coordination environment and long-range interactions. Therefore, the electronic structure of SACs is tunable, which helps to improve the selectivity of the CO₂RR. Also, SACs are ideal models for exploring the structure–activity relationship because of their homogeneous atomically-dispersed metal active centers.

3.2. CO₂ to CO

Various strategies have been developed to promote the catalytic performance of SACs for the CO₂RR to CO, including regulation of the center metal atom and manipulation of the coordination environment of the center metal atom. Recently, great achievements have been made in the production of CO from CO₂ on SACs. But, for commercial applications, further improvements in intrinsic catalytic activity and stability are needed. In this section, the developed strategies to promote the production of CO on SACs *via* the CO₂RR are summarized.

3.2.1. Modulation of the metal atomic center for boosting CO₂ reduction to CO.

SACs with different metal centers possess different d-band centers, which determine their catalytic performance in the CO₂RR. Typically, the higher the d-band center is, the stronger the SAC binds with the intermediates. Jiang *et al.* synthesized various SACs implanted in N-doped carbon (M₁-N-C; M = Fe, Co, Ni, and Cu) by calcining metal-organic frameworks (MOF).⁶⁷ Aberration-corrected high-angle annular dark field scanning transmission electron microscopy (HAADF-STEM) images showed sparsely distributed bright dots, and Fourier transformed extended X-ray absorption fine structure (FT-EXAFS) spectra confirmed the absence of M–M bonds in all SACs, indicating that the metal atoms were atomically dispersed. In the N K-edge near-edge X-ray absorption fine structure (NEXAFS) spectra, a peak was found broadened and split into a doublet (a1 and a2), revealing that the metal atoms were stabilized by pyridinic N. EXAFS fitting results further showed that the metal centers in all SACs were coordinated with four pyridinic N atoms. Besides, all SACs possessed a similar N content and metal loading amount (about 4.94 at% and 1.75 wt%, respectively). Electrochemical results exhibited that Ni₁-N-C had the best activity and selectivity towards CO production, followed by Fe₁-N-C, Co₁-N-C, and Cu₁-N-C. Specifically, the TOF and CO partial current density of Ni₁-N-C reached 11 315 h⁻¹ and 27 mA cm⁻², respectively, at –0.8 V

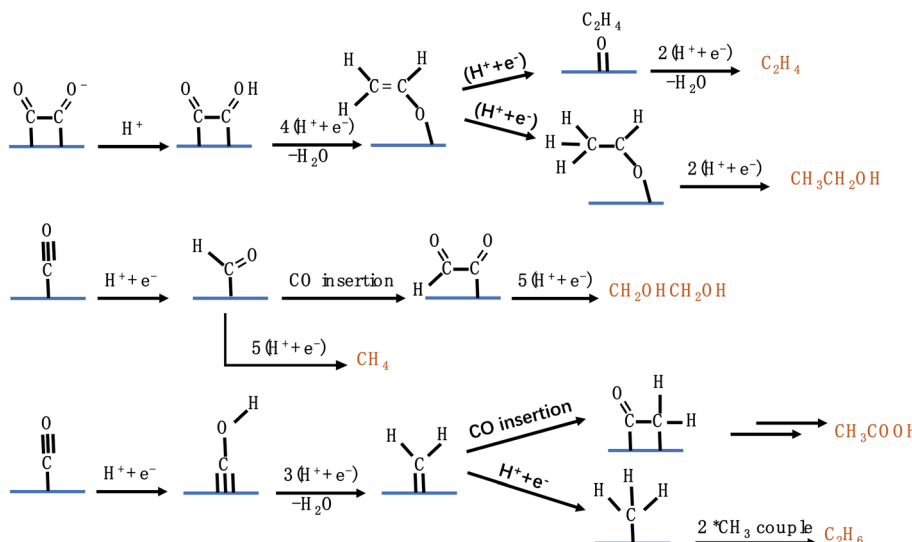


Fig. 5 The possible CO₂RR pathways for C₂ products.



vs. RHE. $\text{Ni}_{1\text{-N-C}}$ displayed a much smaller Tafel slope (98 mV per decade) than the other SACs (104 mV per decade for $\text{Fe}_{1\text{-N-C}}$, 142 mV per decade for $\text{Co}_{1\text{-N-C}}$, and 118 mV per decade for $\text{Cu}_{1\text{-N-C}}$). Additionally, $\text{Ni}_{1\text{-N-C}}$ also showed long-term durability at -0.8 V vs. RHE for 10 h without obvious attenuation in terms of current density and FE_{CO} . Density functional theory (DFT) calculations were performed to explain the differences among these SACs. As stated above, all SACs have similar structural parameters except for the metal centers, and offer an ideal model to study the role of metal atomic centers in CO_2RR performance. The calculated free energy diagram revealed that the formation of $^{*}\text{COOH}$ was the rate-determining step (RDS) for all SACs. $\text{Ni}_{1\text{-N-C}}$ and $\text{Fe}_{1\text{-N-C}}$ had a similar energy barrier for $^{*}\text{COOH}$ formation, lower than that of $\text{Co}_{1\text{-N-C}}$ and $\text{Cu}_{1\text{-N-C}}$. Besides, the energy barrier for CO desorption on $\text{Ni}_{1\text{-N-C}}$ was lower than that on $\text{Fe}_{1\text{-N-C}}$, suggesting favorable CO release from $\text{Ni}_{1\text{-N-C}}$ (Fig. 6a). The $U_{\text{L}}(\text{CO}_2) - U_{\text{L}}(\text{H}_2)$ values for $\text{Ni}_{1\text{-N-C}}$, $\text{Fe}_{1\text{-N-C}}$, $\text{Co}_{1\text{-N-C}}$ and $\text{Cu}_{1\text{-N-C}}$ are -1.19 eV , -1.55 eV , -1.98 eV , and -2.33 eV , respectively. The most positive value of $U_{\text{L}}(\text{CO}_2) - U_{\text{L}}(\text{H}_2)$ for $\text{Ni}_{1\text{-N-C}}$ supported the conclusion that $\text{Ni}_{1\text{-N-C}}$ had the highest selectivity towards CO production (Fig. 6b). Peter *et al.* also prepared a series of transition metal SACs (Fe-N-C , Co-N-C , Ni-N-C , Cu-N-C , and Mn-N-C) and studied their CO_2RR performance.⁶⁸ The results demonstrated that Fe-N-C produced the most CO at low overpotentials, while Ni-N-C produced the most CO at high overpotentials (Fig. 6c). Fe-N-C , Mn-N-C , and Co-N-C all bind to CO^{*} very strongly such that desorption of CO becomes the RDS for these SACs. Ni-N-C and Cu-N-C display a weak binding to $^{*}\text{COOH}$ and thus they require higher overpotentials to initiate the CO_2RR . Interestingly, a small amount of CH_4 was detected in the CO_2RR catalyzed on Fe-N-C and Mn-N-C due to their strong adsorption towards CO^{*} , indicating their potential for producing CH_4 (Fig. 6d). Other studies also attained a similar consensus that the Ni SAC possessed the highest activity and selectivity for the CO_2RR to CO among different SACs.⁶⁹⁻⁷³

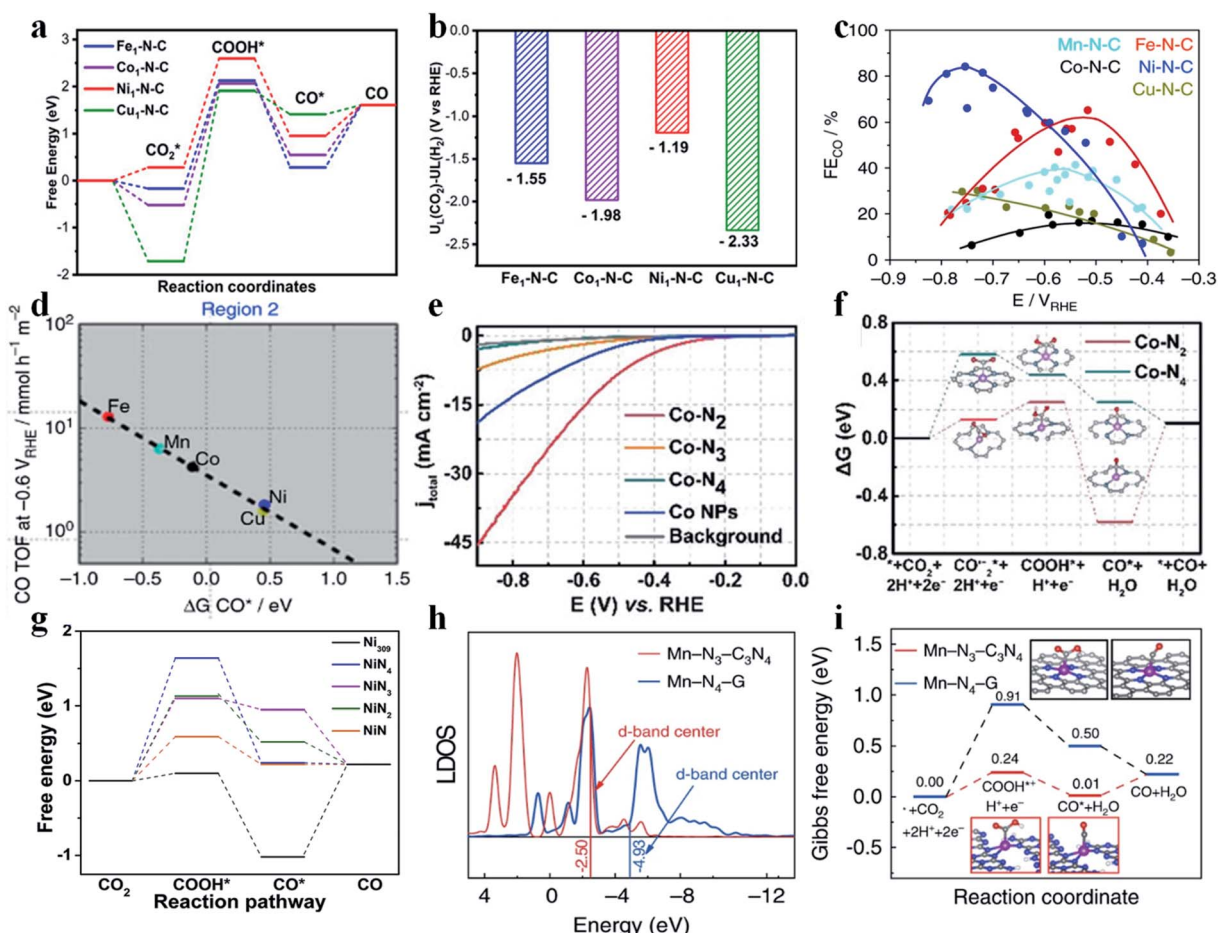


Fig. 6 (a) Calculated free energy diagram of CO_2 reduction to CO and (b) the values of $U_{\text{L}}(\text{CO}_2) - U_{\text{L}}(\text{H}_2)$ for various M1-N-C catalysts. Reproduced with permission from ref. 67. Copyright (2020) Wiley-VCH. (c) FE_{CO} for various SACs at different potentials. (d) TOF_{CO} at -0.6 V vs. RHE as a function of CO free adsorption energy. Reproduced with permission from ref. 68. Copyright (2017) Springer Nature. (e) LSV curves of Co-N_2 , Co-N_3 , Co-N_4 , and Co NPs and pure carbon paper as the background. (f) Calculated Gibbs free energy diagram for CO_2 electro-reduction to CO on Co-N_2 and Co-N_4 . Reproduced with permission from ref. 74. Copyright (2018) Wiley-VCH. (g) Free energy diagram for conversion of CO_2 to CO on a Ni-SAC and Ni_{309} cluster at $U = 0\text{ V}$ vs. RHE. Reproduced with permission from ref. 76. Copyright (2019) Elsevier. (h) Local density of states (LDOS) of Mn in $\text{Mn-N}_3\text{-C}_3\text{N}_4$ and $\text{Mn-N}_4\text{-G}$. (i) Calculated Gibbs free energy diagram for the CO_2RR over $\text{Mn-N}_3\text{-C}_3\text{N}_4$ and $\text{Mn-N}_4\text{-G}$. Reproduced with permission from ref. 77. Copyright (2020) Springer Nature.

3.2.2. Effect of coordination number on CO_2 reduction to CO. Typically, in SACs, the metal atomic center is coordinated with four non-metal atoms. However, this structure does not always give the best CO_2RR activity. Regulating the coordination number in SACs offers an effective strategy to tune the adsorption energy of reaction intermediates and thus their catalytic performance. Generally, the lower the coordination number, the stronger the adsorption of intermediates on SACs. Li *et al.* prepared $\text{Co}-\text{N}_2$, $\text{Co}-\text{N}_3$, and $\text{Co}-\text{N}_4$ by calcining Co/Zn zeolitic imidazolate frameworks (ZIFs) at different temperatures.⁷⁴ Since N species became volatile at high temperature, $\text{Co}-\text{N}_2$, $\text{Co}-\text{N}_3$, and $\text{Co}-\text{N}_4$ could be obtained at 1000 °C, 900 °C, and 800 °C. The atomically dispersed Co atoms could be directly observed by HAADF-STEM. EXAFS confirmed the existence of Co-N bonds (at around 1.4 Å) and the absence of Co-Co bonds. The intensity of the Co-N peak for $\text{Co}-\text{N}_2$ was found much lower than that for $\text{Co}-\text{N}_3$ and $\text{Co}-\text{N}_4$, indicating lower coordination around the Co center in $\text{Co}-\text{N}_2$. EXAFS fitting gave the Co-N coordination number in these Co-SACs of 2.2, 3.1, and 4.1, respectively. Electrochemical measurements showed that $\text{Co}-\text{N}_2$ had the highest activity to reduce CO_2 to CO (Fig. 6e). $\text{Co}-\text{N}_2$, $\text{Co}-\text{N}_3$, and $\text{Co}-\text{N}_4$ have similar structural parameters except the Co-N coordination number, and provide an ideal platform to elucidate the influence of coordination number on CO_2RR performance. DFT calculations disclosed that the endergonic $\text{CO}_2^{\cdot-}\text{*}$ formation was the RDS for these Co-SACs. Owing to the higher d-band center of $\text{Co}-\text{N}_2$ (−0.81 eV) than that of $\text{Co}-\text{N}_4$ (−1.06 eV), $\text{Co}-\text{N}_2$ had a lower energy barrier than $\text{Co}-\text{N}_4$ to form $\text{COO}^{\cdot-}\text{*}$, explaining the higher CO_2RR activity on $\text{Co}-\text{N}_2$ (Fig. 6f). Additionally, the authors further measured the OH^- adsorption strength to simulate the binding affinity of $\text{COO}^{\cdot-}\text{*}$ as $\text{COO}^{\cdot-}\text{*}$ was unstable in the electrolyte. $\text{Co}-\text{N}_2$ showed a more negative OH^- adsorption peak, verifying its stronger adsorption to $\text{COO}^{\cdot-}\text{*}$. Considering the higher catalytic activity of $\text{Co}-\text{N}_4$ towards the HER,⁷⁵ the enhanced CO_2RR performance of $\text{Co}-\text{N}_2$ could also be related to the increase in $U_{\text{l}}(\text{CO}_2) - U_{\text{l}}(\text{H}_2)$. This work indicated that lower coordination number in SACs would enhance the adsorption of CO_2RR intermediates. Li *et al.* performed DFT calculations to study Ni SACs with different coordination numbers (NiN_x ; $x = 1\text{--}4$) toward catalyzing the CO_2RR .⁷⁶ The results show that the RDS for all studied NiN_x SACs is the formation of $\text{COOH}^{\cdot-}$ – an endergonic step. NiN has the lowest coordination number and thus possesses the smallest energy barrier to generate the $\text{COOH}^{\cdot-}$ intermediate, justifying its highest CO_2RR activity (Fig. 6g). Zhang *et al.* synthesized $\text{Mn}-\text{N}_3$ and $\text{Mn}-\text{N}_4$ catalysts and measured their CO_2RR performance. The $\text{Mn}-\text{N}_3$ catalyst delivered a 98.8% CO FE with a CO partial current density of 14 mA cm^{−2} at an overpotential of 0.44 V. *In situ* X-ray absorption spectroscopy showed that $\text{Mn}-\text{N}_3$ facilitated the formation of $\text{COOH}^{\cdot-}$, which is the RDS. DFT calculation gave an energy barrier of 0.24 eV for $\text{Mn}-\text{N}_3$ and 0.91 eV for $\text{Mn}-\text{N}_4$ (Fig. 6i). Local density of states (LDOS) revealed that the d-band centers of $\text{Mn}-\text{N}_3$ and $\text{Mn}-\text{N}_4$ were located at −2.50 eV and −4.93 eV, respectively (Fig. 6h).⁷⁷ Other researchers also reached a similar conclusion that the lower coordination number in SACs indeed strengthened the adsorption of CO_2RR intermediates.^{78–83}

3.2.3. Effect of the coordinated nitrogen type on CO_2 reduction to CO. Four types of nitrogen atoms exist in SACs,

namely pyridinic, pyrrolic, graphitic and oxidized N. The metal centers in SACs could be bonded with pyridinic N or pyrrolic N. The d-band center for pyrrolic-N coordinated metal sites is lower than that for pyridinic-N coordinated metal sites and thus pyrrolic-N coordinated metal sites bind to the CO_2RR intermediates more weakly. Hu *et al.* prepared $\text{Fe}^{3+}\text{-N-C}$ coordinated with pyrrolic N and $\text{Fe}^{2+}\text{-N-C}$ coordinated with pyridinic N using different pyrolysis precursors.⁸⁴ $\text{Fe}^{3+}\text{-N-C}$ could reduce CO_2 to CO with a CO partial current density of 94 mA cm^{−2} at an overpotential of 340 mV. No catalytic performance decay was observed in 12 hours of continuous reaction. *Operando* X-ray absorption spectroscopy verified the true active sites of Fe^{3+} ions coordinated with pyrrolic N atoms and the +3 oxidation state of Fe was maintained during the reaction (Fig. 7a). Furthermore, electrochemical measurements indicated that the faster CO_2 activation and weaker CO adsorption were responsible for the superior catalytic activity of $\text{Fe}^{3+}\text{-N-C}$. Other research groups also regarded M-pyrrolic N as the active center for the CO_2RR .^{85,86} Wang *et al.* constructed $\text{Co}(\text{II})\text{CPY}$ (Co atoms coordinated with four pyridinic N atoms) and Co-porphine (Co atoms coordinated with four pyrrolic N atoms) and found that $\text{Co}(\text{II})\text{CPY}$ showed better CO_2RR activity than Co-porphine.⁸⁷ DFT calculations suggested that the formation of $\text{COOH}^{\cdot-}$ was the RDS, in which $\text{Co}(\text{II})\text{CPY}$ had a lower energy barrier (Fig. 7b). Bader charge analysis showed that the Co atoms in $\text{Co}(\text{II})\text{CPY}$ could get more electrons from the ligand compared with the case in Co-porphine (Fig. 7c). Projected density of states (PDOS) demonstrated that the d_{z^2} orbital of $\text{Co}(\text{II})\text{CPY}$ was closer to the Fermi level before the reaction and had a larger overlap with the 2p orbital of COOH after the reaction, substantiating the enhancement of $\text{COOH}^{\cdot-}$ adsorption in $\text{Co}(\text{II})\text{CPY}$. Other research studies also reached the same conclusion that M-pyridinic N species served as the reaction sites in catalyzing the CO_2RR .^{72,73,88–91} Since the controversy about which type of M-N species is the active site(s) in the CO_2RR still remains, more attention has to be paid on this research hotspot.

3.2.4. Effect of heteroatoms on CO_2 reduction to CO.

Heteroatom doping could induce electron transfer between the metal atomic center and the surrounding non-metal atoms, leading to the distinct electronic structure and hence the electrocatalytic performance. Liu *et al.* synthesized a S doped Ni-SAC ($\text{Ni}-\text{N}_3\text{S}$) and $\text{Ni}-\text{N}_4$ and studied their CO_2RR mechanisms.⁹² The CO_2RR onset potential of $\text{Ni}-\text{N}_3\text{S}$ was 100 mV lower than that of $\text{Ni}-\text{N}_4$. *Operando* XAS showed that the valence state of Ni atoms in Ni SACs was +1, serving as the true active sites. Moreover, the Ni^+ sites were identified as having strong interactions with CO_2 , where electrons were transferred from Ni^+ to the C 2p orbital in CO_2 to generate $\text{CO}_2^{\cdot-}$, facilitating the CO_2 activation and further reduction (Fig. 7d). Consequently, the catalyst achieved a specific current of 350 A g_{catalyst}^{−1} and a TOF of 14 800 h^{−1} at an overpotential of 0.61 V with 97% FE_{CO}. The authors also proposed the activation process of CO_2 on the Ni(i) active center and its structural evolution during the CO_2RR (Fig. 7d). Cl doping in a Mn-SAC was reported by Zhang *et al.* to improve the CO_2RR activity. Mn-SACs usually displayed poor selectivity towards CO production because of their too strong adsorption for CO^* , making CO release rather difficult. After



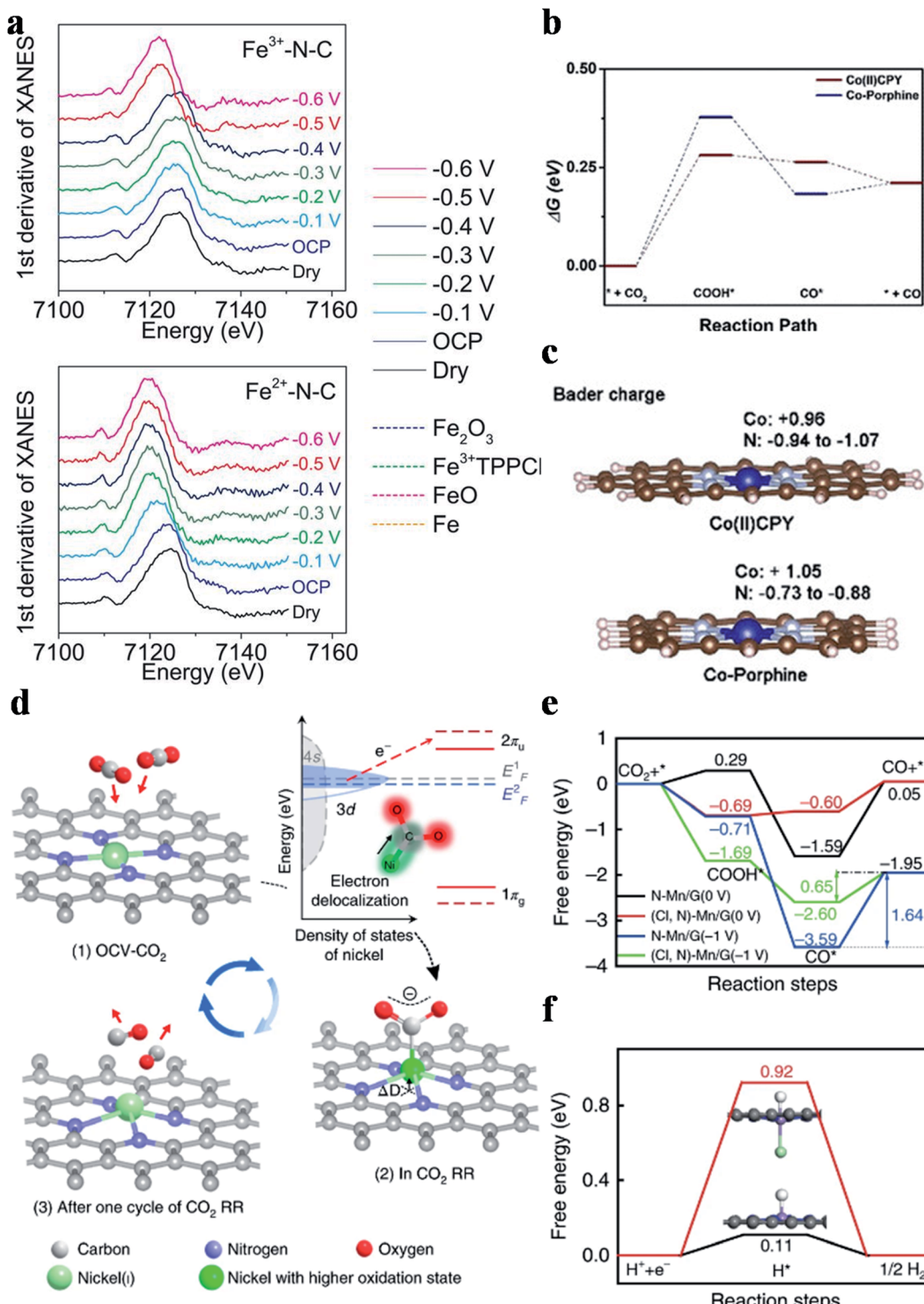


Fig. 7 (a) The first derivative of the XANES spectra for Fe³⁺-N-C and Fe²⁺-N-C as dry powder (black) and on a glassy carbon electrode at the open circuit potential (OCP) (blue), -0.1 V (light blue), -0.2 V (green), -0.3 V (dark green), -0.4 V (dark blue), -0.5 V (red), and -0.6 V (pink) versus RHE, with Fe₂O₃ (blue dashed), Fe³⁺TPPCL (green dashed), FeO (pink dashed), and Fe foil (orange dashed) references. Reproduced with permission from ref. 84. Copyright (2019) the American Association for the Advancement of Science. (b) Free energy profiles of Co(II)CPY/Graphene and Co-porphine/Graphene. Reproduced with permission from ref. 87. Copyright (2020) Wiley-VCH. (c) Bader charge of Co and N atoms. Reproduced with permission from ref. 92. Copyright (2018) Springer Nature. (e) Calculated free energy of the CO₂RR. (f) Calculated free energy of hydrogen adsorption. Reproduced with permission from ref. 93. Copyright (2019) Springer Nature.

introducing Cl into the Mn-SAC ((Cl, N)-Mn/G), the selectivity towards CO was significantly increased from 17% to 97% with the partial current density for CO production exhibiting an 11-fold increase. PDOS revealed that the d-band center of (Cl, N)-Mn/G was lower than that of MnN₄, weakening the CO* adsorption and thus improving the CO selectivity. The free energy diagram further supported this conclusion. Specifically, the energy barrier of the RDS (desorption of CO*) decreased from 1.64 eV for MnN₄ to 0.65 eV for (Cl, N)-Mn/G (Fig. 7e). Moreover, the energy barrier for H₂ generation increased from 0.11 eV for MnN₄ to 0.92 eV for (Cl, N)-Mn/G, implying that the HER was largely suppressed (Fig. 7f).⁹³

3.2.5. Effect of dual metal atoms on CO₂ reduction to CO.

Although much progress has been made in the CO₂RR to

produce CO using SACs, their performance could be further improved through constructing dual metal atomic sites. Gong *et al.* demonstrated an example of neighboring Zn and Co monomers (ZnCoNC) for enhancing CO production in the CO₂RR.⁹⁴ ZnCoNC displayed a CO FE of 93.2% at -0.5 V vs. RHE in 30 h. XANES confirmed the interaction between Zn and Co. According to the free energy diagram, after introducing Co into the Zn-SAC, the formation of COOH* (the RDS for the Zn-SAC) changed from endergonic to exergonic (Fig. 8a), which enhanced the adsorption of COOH* and thus promoted CO production. Zhao *et al.* synthesized a Ni-Fe dual-metal-atom catalyst (NiFe-N-C).⁹⁵ Electrochemical study disclosed that NiFe-N-C possessed higher activity and selectivity than Ni-N-C and Fe-N-C in the CO₂RR (Fig. 8b and c). The calculated free

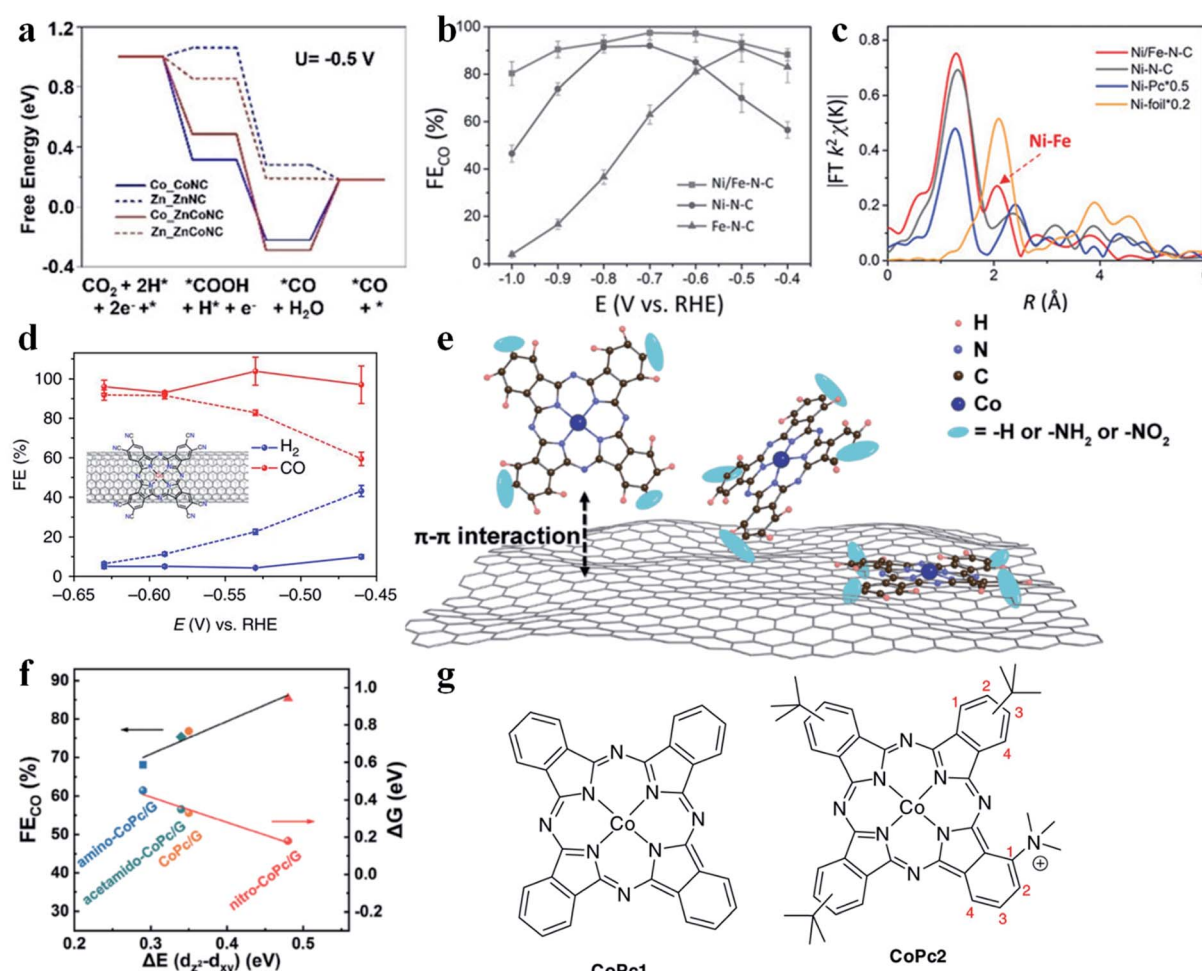


Fig. 8 (a) Calculated free energy for CO₂ reduction to CO. Reproduced with permission from ref. 94. Copyright (2020) Wiley-VCH. (b) FE of CO for various SACs. (c) Fourier transformation of the EXAFS spectra at R space. Reproduced with permission from ref. 95. Copyright (2019) Wiley-VCH. (d) Faradaic efficiencies of reduction products at different potentials for CoPc-CN/CNT (solid line) in comparison with CoPc/CNT (dotted line). The inset in (d) shows the molecular structure of CoPc-CN, which is anchored on a CNT. The average values and error bars in (e) are based on six measurements during three reaction runs (two product analysis measurements were performed in each run). The error bars represent standard deviation of six measurements. The data are all iR corrected. Reproduced with permission from ref. 97. Copyright (2017) Springer Nature. (e) Schematic illustration showing the construction of single cobalt atom catalysts for the CO₂RR. (f) The linear relationship between the CO faradaic efficiency/Gibbs free energy of CO₂ reduction to the *CO₂⁻ intermediate and the energy difference $\Delta E(d_{z^2} - d_{xy})$. Reproduced with permission from ref. 96. Copyright (2020) Springer. (g) CoPc1 (left) bears no substituents, and CoPc2 (right) bears one trimethyl ammonium group at position 1 of the isoindole subunits, and three *tert*-butyl groups (position 2 or 3) of the other subunits. Reproduced with permission from ref. 98. Copyright (2019) Springer Nature.



energy diagram showed that the energy barrier for COOH^* formation (RDS) was much lower in NiFe-N-C than in Ni-N-C. Therefore, Fe doping could strengthen the binding affinity of Ni atoms for COOH^* . It is worth mentioning that two mechanisms are possible for enhancing the CO_2RR performance in dual metal atom catalysts. One is that only one metal site acts as the active center, and the introduction of the second metal atom regulates the electronic structure of the first metal site. The other is that both metal sites serve as the active centers for adsorbing reaction intermediates and engage in the reaction. To date, the reported examples belong to the former mechanism. If the reaction could follow the latter mechanism on dual metal atom catalysts, the scaling relationship might be broken, which provides another possibility to tune the CO_2RR performance.

3.2.6. Effect of surrounding functional groups on CO_2 reduction to CO. The charge state of the metal atomic center

determines its intrinsic catalytic activity. Therefore, introducing functional groups (electron-withdrawing or electron-donating) into SACs offers an effective strategy to manipulate their CO_2RR performance. Huang *et al.* prepared CoPc/G, amino functionalized CoPc/G (amino-CoPc/G), and nitro functionalized CoPc/G (nitro-CoPc/G) and studied the effect of electron-withdrawing/electron-donating groups in SACs on the CO_2RR activity (Fig. 8e).⁹⁶ Electrochemical measurements showed that nitro-CoPc/G possessed the highest activity and selectivity for generating CO. DFT calculations revealed that formation of $^*\text{CO}_2^-$ was the RDS, where nitro-CoPc/G had the lowest energy barrier. After the introduction of the electron-withdrawing nitro group, the electron density around the Co site decreased. Also, the d_{z^2} orbital was upshifted and became less affected by other lower energy level orbitals, like d_{xy} . Another important descriptor was also found, that is, the larger the energy difference between the d_{z^2} and d_{xy} orbital, the smaller the energy

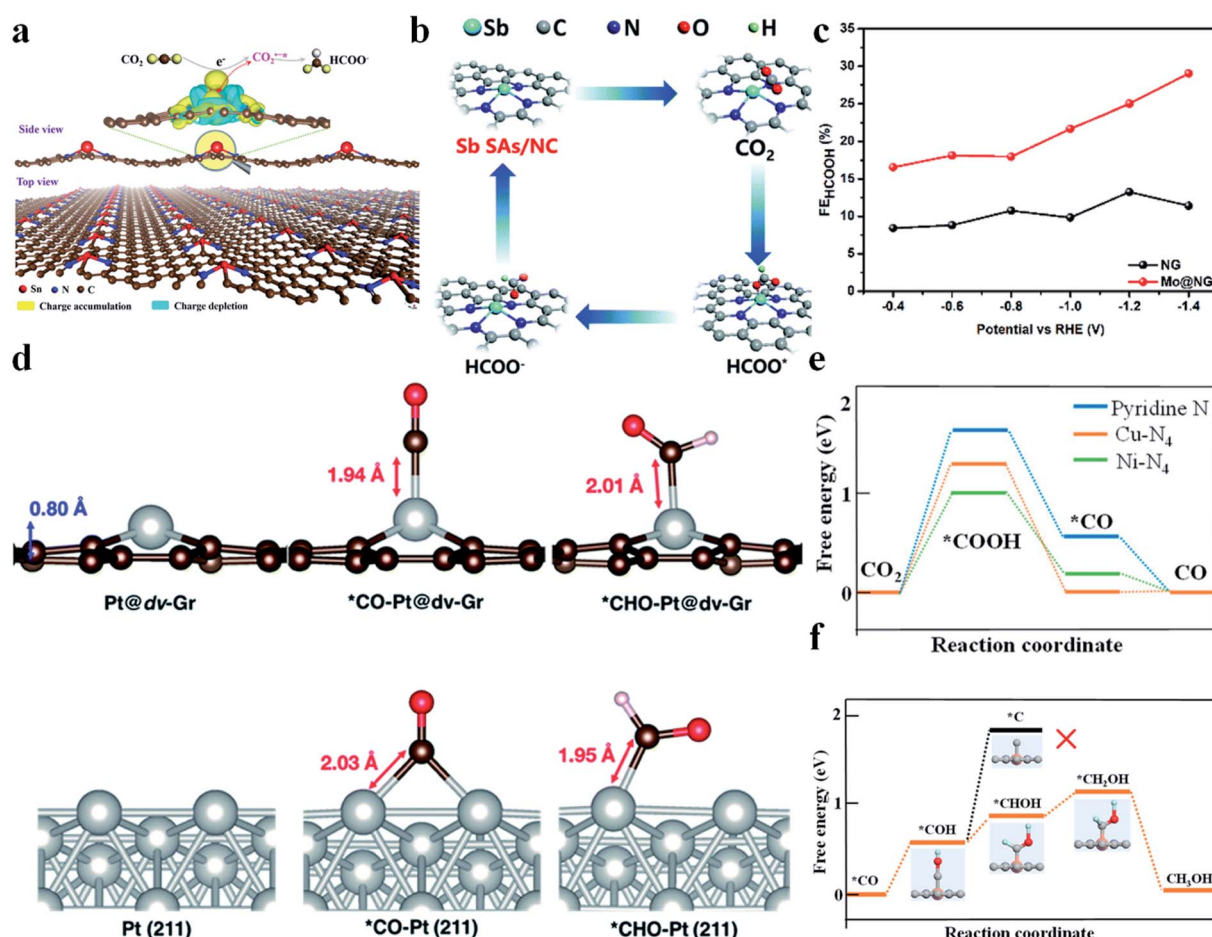


Fig. 9 (a) Plot showing 3D differential charge density of single $\text{Sn}^{\delta+}$ atoms on N-doped graphene and the schematic illustration of CO_2 electroreduction into formate. The yellow and blue isosurfaces correspond to the increase and depletion in the number of electrons, respectively. Reproduced with permission from ref. 99. Copyright (2019) Wiley-VCH. (b) Proposed CO_2RR mechanism on Sb SA/NC. Reproduced with permission from ref. 101. Copyright (2020) The Royal Society of Chemistry. (c) Comparison of formate faradaic efficiency between NG and Mo@NG. Reproduced with permission from ref. 102. Copyright (2019) Elsevier. (d) Optimized geometries of Pt@dv-Gr and Pt (211) before and after adsorption of $^*\text{CO}$ and $^*\text{CHO}$. Reproduced with permission from ref. 7. Copyright (2017) The Royal Society of Chemistry. (e) Free energy diagram of CO_2 reduction to CO on pyridine N, Ni-N₄, and Cu-N₄. Orange, gray, dark blue, red, and light blue spheres stand for Cu, C, N, O, and H atoms, respectively. Reproduced with permission from ref. 105. Copyright (2019) American Chemical Society.



barrier to form $^*\text{CO}_2^-$ (Fig. 8f). Wang *et al.* introduced an electron-withdrawing cyano group into CoPc/CNT (CoPc-CN/CNT) and found that both activity and CO selectivity increased obviously (Fig. 8d).⁹⁷ The electron-withdrawing cyano group could prompt the generation of Co(i), which was regarded as the active site for the CO_2RR . The enhanced Co(II)/Co(i) redox transition at more positive potentials in CoPc-CN/CNT supported this proposal. Moreover, the cyano group also reduced the affinity of the Co site for CO^* , facilitating the release of CO. In addition to the nitro group and cyano group, a trimethyl ammonium group (CoPc2) was also introduced into CoPc1 (Fig. 8g).⁹⁸ After such a modification, the CoPc2 showed high selectivity towards CO production, while the CO partial current density increased substantially.

3.3. HCOOH

It is reported that SACs with a p-block metal (Sn, Sb) center are able to catalyze the CO_2RR to produce formic acid or formate. Xie *et al.* synthesized SnN_2C_2 and found that it could reduce CO_2 to formate at a very low onset overpotential of 60 mV and with a high TOF of $11\,930\text{ h}^{-1}$ at -1.14 V vs. RHE .⁹⁹ Moreover, its activity did not decay during 200 h of continuous reaction. DFT calculations revealed that electrons were transferred from Sn atoms to graphene, making Sn atoms positively charged. Fourier transformed infrared spectroscopy (FTIR) spectra and Gibbs free energy calculations confirmed that $\text{Sn}^{\delta+}$ could facilitate CO_2 activation and protonation through stabilizing $\text{CO}_2^{\cdot-*}$ and $\text{HCOO}^{\cdot-*}$ (Fig. 9a). Wei *et al.* constructed a NiSn atomic pair (NiSn-APC) and also achieved a good performance in the CO_2RR to formate.¹⁰⁰ NiSn-APC produced HCOOH with a high TOF of 4752 h^{-1} and formate productivity of $36.7\text{ mol h}^{-1}\text{ g}_{\text{Sn}}^{-1}$ at -1.02 V vs. RHE . *In situ* attenuated total reflection-infrared (ATR-IR) spectra and theoretical calculations confirmed the electron redistribution on Sn, which is induced by the adjacent Ni atoms. Moreover, ΔG ($^*\text{HCOOH}$) (-0.05 eV) was much smaller than ΔG ($^*\text{COOH}$) (1.36 eV), explaining its high selectivity towards formate production. Sb-N₄ (Sb SA/NC) reported by Li's group also displayed a good CO_2RR performance.¹⁰¹ Sb SA/NC produced formate with a FE of 94% at -0.8 V vs. RHE . *In situ* XAFS and DFT calculations verified that the positively charged $\text{Sb}^{\delta+}\text{-N}_4$ was the origin of the high catalytic activity. Sb SA/NC possessed a ΔG (HCOO^*) (0.21 eV) smaller than ΔG (COOH^*) (1.00 eV) and ΔG (H^*) (0.81 eV), implying that formate production was more favorable than CO and H_2 (Fig. 9b). Xie *et al.* reported that Mo atoms supported on N doped graphene (Mo@NG) could also efficiently reduce CO_2 to produce HCOOH. Mo@NG generated HCOOH with a high FE, twice as that of NG, and achieved a formate yield of $747\text{ mmol g}_{\text{catalyst}}^{-1}\text{ h}^{-1}$ (Fig. 9c).¹⁰²

3.4. CH_3OH

CH_3OH is a high value-added product in the CO_2RR . However, as discussed above, both CO_2RR pathways to generate CH_3OH ($^*\text{CH}_2\text{OH}$ and $^*\text{CH}_3\text{O}$) possess very high energy barriers and thus its production remains a big challenge. Wang *et al.* immobilized cobalt phthalocyanine (CoPc) onto carbon

nanotubes (CNTs), denoted as CoPc/CNT.¹⁰³ CoPc/CNT was found to be able to reduce CO_2 to CH_3OH with a FE of 44% and a partial current density greater than 10 mA cm^{-2} at -0.94 V vs. RHE . But the catalytic activity of CoPc/CNT quickly decayed after 1 h of electrochemical reaction. To enhance the stability, an amino functional group was introduced into CoPc/CNT to form CoPc-NH₂/CNT, whose stability was greatly improved. In addition to experiments, theoretical studies have also been conducted to prompt the discovery of potential catalysts to reduce CO_2 to CH_3OH . Cai *et al.* anchored Co, Rh, and Ir atoms onto porphyrin-like graphene.¹⁰⁴ First, the structural stability of the SACs was confirmed from the strong hybridization between metal d-orbitals and N 2p-orbitals. Then, the energy barriers for the CO_2RR to CH_3OH were calculated. CoN₄/graphene was found most promising among the three studied catalysts for CH_3OH generation with a RDS energy barrier of only 0.59 eV . Jung *et al.* conducted DFT calculations to predict a series of transition metal SACs on graphene with single and double vacancies.⁷ They figured out that Ni and Pt SACs with double vacancies (Ni@dv-Gr, Pt@dv-Gr) were promising to reduce CO_2 to CH_3OH . Taking Pt@dv-Gr as an example, CO^* was adsorbed on one Pt atom *via* the top-on adsorption configuration, while bulk Pt adsorbed CO^* *via* two Pt atoms adopting the bridge adsorption mode. As a result, bulk Pt adsorbed CO^* so strongly that the transformation of CO^* to $^*\text{CHO}$ – an important intermediate for CH_3OH formation – became rather difficult. In contrast, Pt@dv-Gr had a much smaller energy barrier for this step and held the premise for CH_3OH production (Fig. 9d). He *et al.* developed a simple method to prepare a Cu-SAC on through-hole carbon nanofibers (Cu SAs/TCNFs).¹⁰⁵ The Cu SAs/TCNFs (Cu-N₄) could generate methanol with a FE of 44%. DFT calculations found that the energy barrier for COOH^* formation was much larger than that for CHOH^* formation on Cu-N₄, which effectively suppressed the CO production. Moreover, Cu-N₄ could adsorb CO^* more strongly than Ni-N₄, which allowed CO^* to be further reduced (Fig. 9e). Additionally, the energy barrier to form C^* from COH^* , an important step towards CH_4 , was calculated to be 1.88 eV , which is much larger than that to form CH_3OH (Fig. 9f). Therefore, CH_3OH was more favorable than CH_4 in the CO_2RR . In summary, the mechanism of the CO_2RR to form CH_3OH on SACs was nearly completely based on DFT calculation. The lack of understanding of the structural characteristics poses a big challenge for designing efficient SACs for reducing CO_2 to CH_3OH .

3.5. CH_4

CH_4 is another important product in the CO_2RR , which undergoes an 8e^- transfer process. Strong adsorption affinity of metal sites for the CO^* intermediate is required for generating CH_4 . Xin *et al.* reported Zn-N₄ that could stably reduce CO_2 to CH_4 with a FE of 85% and a partial current density of -31.8 mA cm^{-2} at $-1.8\text{ V vs. the saturated calomel electrode (SCE)}$ (Fig. 10a-c).¹⁰⁶ DFT calculations showed that Zn atoms tended to bond with O atoms to form $^*\text{OCHO}$ (ΔG ($^*\text{OCHO}$) = 0.46 eV) rather than with C atoms to form COOH^* (ΔG ($^*\text{COOH}$) = 1.2 eV) (Fig. 10d). Furthermore, surface-enhanced infrared

absorption spectroscopy enabled direct observation of the existence of $^*\text{OCH}_3$ and $^*\text{OCH}_2$. Zheng *et al.* deposited Cu atoms on CeO_2 nanorods ($\text{Cu}-\text{CeO}_2$), where Cu atoms were stabilized by three oxygen vacancies. $\text{Cu}-\text{CeO}_2$ could reduce CO_2 into CH_4 with a FE of 58% (Fig. 10e and f).¹⁰⁷ Theoretical calculations revealed that the synergistic effect between atomic dispersion of Cu and multiple surrounding oxygen vacancies as well as the contribution from the CeO_2 framework expedited CO_2 adsorption and activation.

3.6. C_{2+}

Generation of C_{2+} products in the CO_2RR requires C-C coupling, which possesses a high energy barrier and is difficult to take place in SACs. Cu nanoparticles have been shown as an

excellent catalyst to reduce CO_2 to form C_{2+} products, while this is not the case for Cu SACs due to the lack of neighbouring active sites to allow for C-C coupling. Fontecave *et al.* reported that a Cu SAC ($\text{Cu}_{0.5}\text{NC}$) could reduce CO_2 to ethanol with a FE of 43% at -1.2 V vs. RHE in 0.1 M CsHCO_3 solution.¹⁰⁸ A higher $\text{FE}_{\text{ethanol}}$ ($\sim 66\%$) could be achieved using CO as the feed gas, suggesting that CO^* might be the important intermediate to form ethanol. *Operando* XAS analysis showed that the initial isolated Cu atoms would aggregate and form Cu NPs during the CO_2RR , acting as the true active sites. Interestingly, Cu atoms could be recovered after the reaction, indicating that such a transition was reversible. Xu *et al.* also observed a similar phenomenon where Cu atoms transformed into Cu_n clusters ($n = 3$ and 4) during the electrochemical reaction and then returned back to their initial state after the reaction.¹⁰⁹ Chen

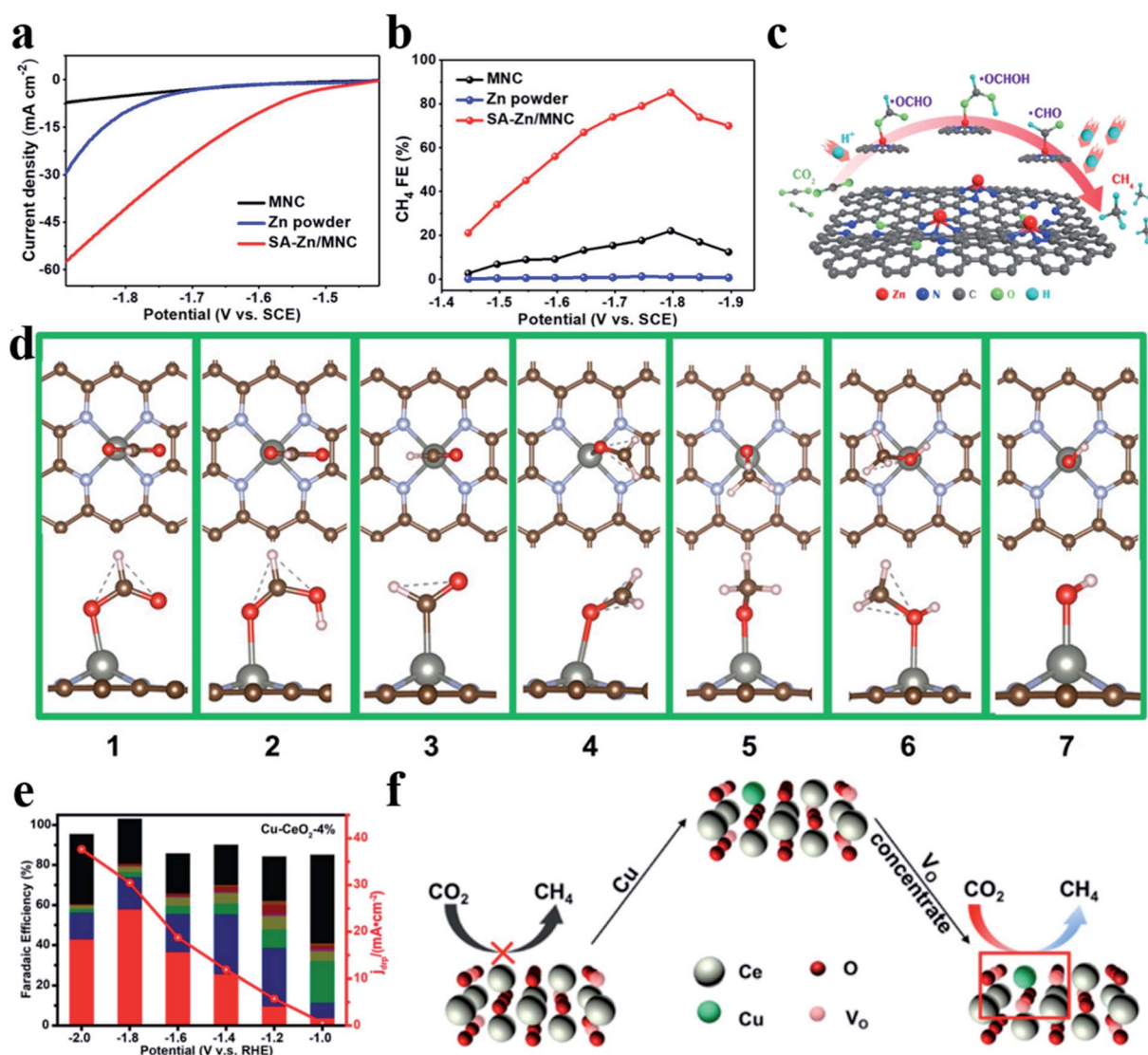


Fig. 10 (a) Polarization curves for MNC, Zn powder, and SA-Zn/MNC. (b) FE for the electrochemical CO_2RR to CH_4 at different applied potentials. (c) CO_2RR pathway for single Zn atoms to produce CH_4 . (d) The most stable structure. The red and pink balls represent O and H atoms, respectively. Reproduced with permission from ref. 106. Copyright (2020) American Chemical Society. (e) Faradaic efficiencies (bars, left y-axis) and the deep reduction product current density (j_{drop} , red curve, right y-axis) of $\text{Cu}-\text{CeO}_2$ -4%. The red column represents CH_4 . (f) Effect of oxygen vacancies on the CO_2RR . Reproduced with permission from ref. 107. Copyright (2018) American Chemical Society.



et al. designed a Cu SAC loaded on N-doped porous carbon (Cu-SA/NPC) to reduce CO_2 into C_{2+} products.¹¹⁰ Cu-SA/NPC produced acetone with a FE of 36.7% and a yield of 336.1 $\mu\text{g h}^{-1}$ at -0.36 V vs. RHE. Theoretical calculations pointed out that Cu coordinated with four pyrrolic N atoms was the true active center, which decreased the energy barrier of CO_2 activation and C-C coupling. Also, the most possible pathway to form acetone was proposed: $\text{CO}_2 \rightarrow \text{COOH}^* \rightarrow \text{CO}^* \rightarrow \text{COCO}^* \rightarrow \text{COCOH}^* \rightarrow \text{COC}^* \rightarrow \text{COCH}^* \rightarrow \text{COCH}_2^* \rightarrow \text{COCH}_3^* \rightarrow \text{COCOCH}_3^* \rightarrow \text{COHCOCH}_3^* \rightarrow \text{CCOCH}_3^* \rightarrow \text{CHCOCH}_3^* \rightarrow \text{CH}_2\text{COCH}_3^* \rightarrow \text{CH}_3\text{COCH}_3$ (Fig. 11a). Zheng *et al.* regulated the population of Cu- N_x sites on NC (Cu-N-C) by controlling the pyrolysis temperature (800 °C and 900 °C), where Cu-N-C-800 contained 4.9 mol% metal atoms and Cu-N-C-900 had 2.4 mol% metal atoms. Adjacent Cu- N_2 sites existed among the densely distributed Cu- N_x in Cu-N-C-800, enabling C-C coupling for C_2H_4 formation with a FE of 24.8% at -1.4 V vs. RHE (Fig. 11b).¹¹¹ DFT calculations disclosed that Cu- N_2 bound with CO^* more strongly (-1.17 eV) than Cu- N_4 (-0.19 eV), which was favorable for CO^* to participate in the further reaction. Moreover, the adjacent Cu- N_2 sites possessed a much lower energy barrier for C-C coupling (0.14 eV) than the isolated Cu- N_2 (1.38 eV). Cu-N-C-900 with fewer neighboring Cu- N_2 sites generated much less C_2H_4 , substantiating the important role of

the adjacent Cu- N_2 sites in C-C coupling. Qiao *et al.* came up with a novel dual active center mechanism to produce C_{2+} products in the CO_2RR , where Cu atoms bound with reaction intermediates having carbon as the anchoring atom ($^*\text{COOH}$, $^*\text{CO}$, and $^*\text{CHO}$) and C atoms on C_3N_4 bound with reaction intermediates having oxygen as the anchoring atom ($^*\text{OCH}_2$, $^*\text{OCH}_3$, $^*\text{O}$, and $^*\text{OH}$) (Fig. 11c).¹¹² The detection of various C_{2+} products validated the reaction mechanism, though the selectivity of C_{2+} products was low (Fig. 11d).

Tandem catalysis provides another efficient strategy to produce C_{2+} products *via* the CO_2RR , in which plenty of CO^* is first generated on one type of active site and it diffuses to the other type of active site, and then gets further reduced to produce C_{2+} products. Grätzel *et al.* fabricated a $\text{Cu}_2\text{O}-\text{Ag}$ tandem catalyst. CO^* was first produced on the Ag sites and then underwent C-C coupling on the Cu sites to generate C_2H_4 . *Operando* Raman spectroscopy allowed direct observation of the enhanced coverage of CH-containing intermediates (Fig. 12a).¹¹³ Consequently, the partial current density of C_2H_4 reached -18.1 mA cm^{-2} at -1.05 V vs. RHE on the CuAg catalyst, while it was -8.5 mA cm^{-2} on the Cu catalyst. A similar tandem catalyst was demonstrated using Ni SAC as the CO generator.¹¹⁴ By optimizing the loading amount of Ni-N-C, the Cu/Ni-N-C tandem electrode could reduce CO_2 into C_{2+}

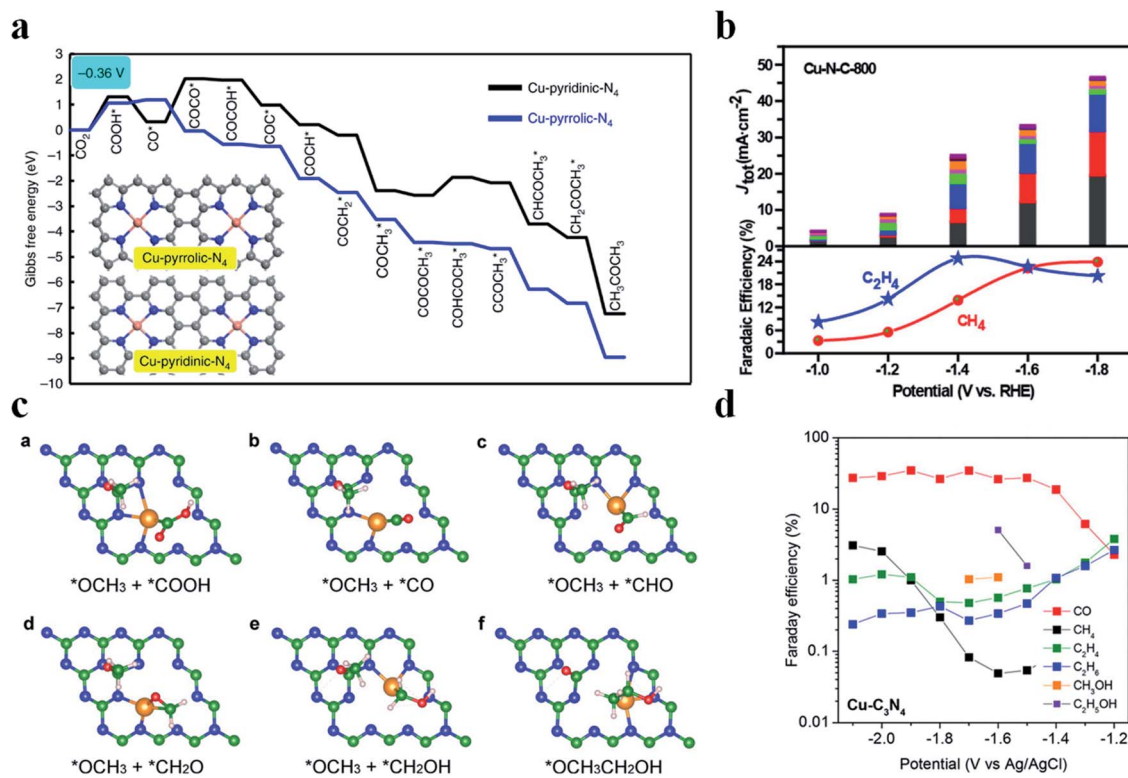


Fig. 11 (a) Free energy diagrams calculated at a potential of -0.36 V vs. RHE for CO_2 reduction to CH_3COCH_3 on Cu-pyridinic- N_4 and Cu-pyrrolic- N_4 sites of Cu-SA/NPC (the computational models are included in the figure). Reproduced with permission from ref. 110. Copyright (2020) Springer Nature. (b) CO_2 electroreduction performance of the Cu-N-C-800 catalyst. Top panel: current densities, with colors indicating different products as shown at the bottom. Bottom panel: faradaic efficiencies of C_2H_4 and CH_4 . Reproduced with permission from ref. 111. Copyright (2020) American Chemical Society. (c) Key reaction intermediates for $\text{CH}_3\text{CH}_2\text{OH}$ generation on Cu- C_3N_4 . (d) The measured faradaic efficiencies of various products on Cu- C_3N_4 at different overpotentials. Reproduced with permission from ref. 112. Copyright (2017) American Chemical Society.

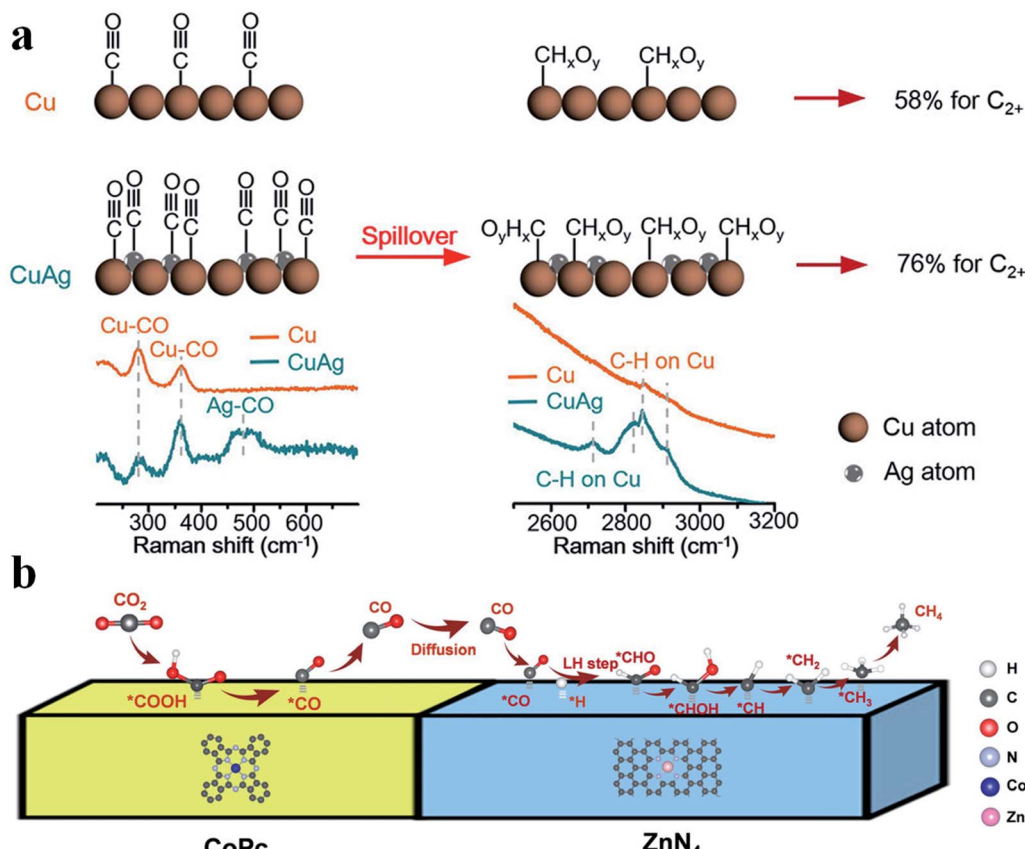


Fig. 12 (a) CO₂RR mechanism for producing C₂₊ products on Cu and CuAg catalysts. Reproduced with permission from ref. 113. Copyright (2019) American Chemical Society. (b) A proposed reaction mechanism of the CO₂RR to CH₄ over CoPc@Zn-N-C. Reproduced with permission from ref. 116. Copyright (2020) Wiley-VCH.

products at a high production efficiency (80% FE) and rate (over 500 mA cm⁻²) (Fig. 13a–c).¹¹⁵ Therefore, the tandem catalysis strategy not only efficiently promoted the C₂₊ product faradaic efficiency, but also substantially enhanced the reaction rate. Wang *et al.* reported that CoPc@Zn-N-C was able to reduce CO₂ to CH₄ *via* a two-step tandem reaction.¹¹⁶ CO was first generated on CoPc, and then it was further reduced to CH₄ on the Zn-N₄ site. DFT calculations disclosed that CoPc not only engaged in the first step to produce CO but also took part in the next step, where it increased the availability of H* over nearby N sites in Zn-N₄ and thus benefited CH₄ formation (Fig. 12b). The above studies highlighted that multiple sites are essential for multi-electron product formation in the CO₂RR, in which the multiple sites can be adjacent single atom sites, or metal atoms and coordination atoms.

The mechanism of the CO₂RR to C₂₊ products on Cu-based catalysts is still controversial due to the multiple electron transfer and dynamic structural transformation in the reaction. The above-mentioned challenges are also present for Cu-N-C SACs. A few studies reported that C₂₊ could be produced by Cu-N-C SACs due to the strong adsorption of CO₂ reduction intermediates on Cu atoms, which is favorable for the C–C coupling. For example, some groups showed that C₂₊ formation was catalyzed by small Cu nanoparticles or clusters in Cu-N-C

SACs, which came from aggregation of Cu single atoms under negative bias. But others reported that Cu single atoms were stable in the CO₂RR, and the formation of the C₂₊ products was on the dual active sites (Cu and N in Cu-N-C SACs). Based on the reported results, the stability of Cu-N-C SACs in the CO₂RR seems to be related to the synthesis method and electrochemical reaction environment, which is directly correlated to the binding strength of Cu single atoms with the substrate. Therefore, it is crucial to develop novel strategies to enhance the binding strength between the central metal atom and the substrate for further studying the reaction mechanism of the CO₂RR to C₂₊ products on SACs. Right now, besides the Cu-N-C SAC, there are no other reported SACs capable of reducing CO₂ to form C₂₊ products. As Zn and Co could strongly adsorb CO₂RR intermediates, combining Zn and Co together to develop a Zn and Co diatomic catalyst might facilitate the reduction of CO₂ to form C₂₊ products.

SACs supported on metals belong to single-atom alloys and some reviews have already summarized their progress.^{117,118} Here, we focus on SACs supported on carbon-based substrates. Besides carbon, other substrates have also been used to support metal single atoms. For example, Li *et al.* deposited Ag single atoms on MnO₂ and found that Ag single atoms in Ag₁/MnO₂ had a higher electronic density close to the Fermi level than Ag

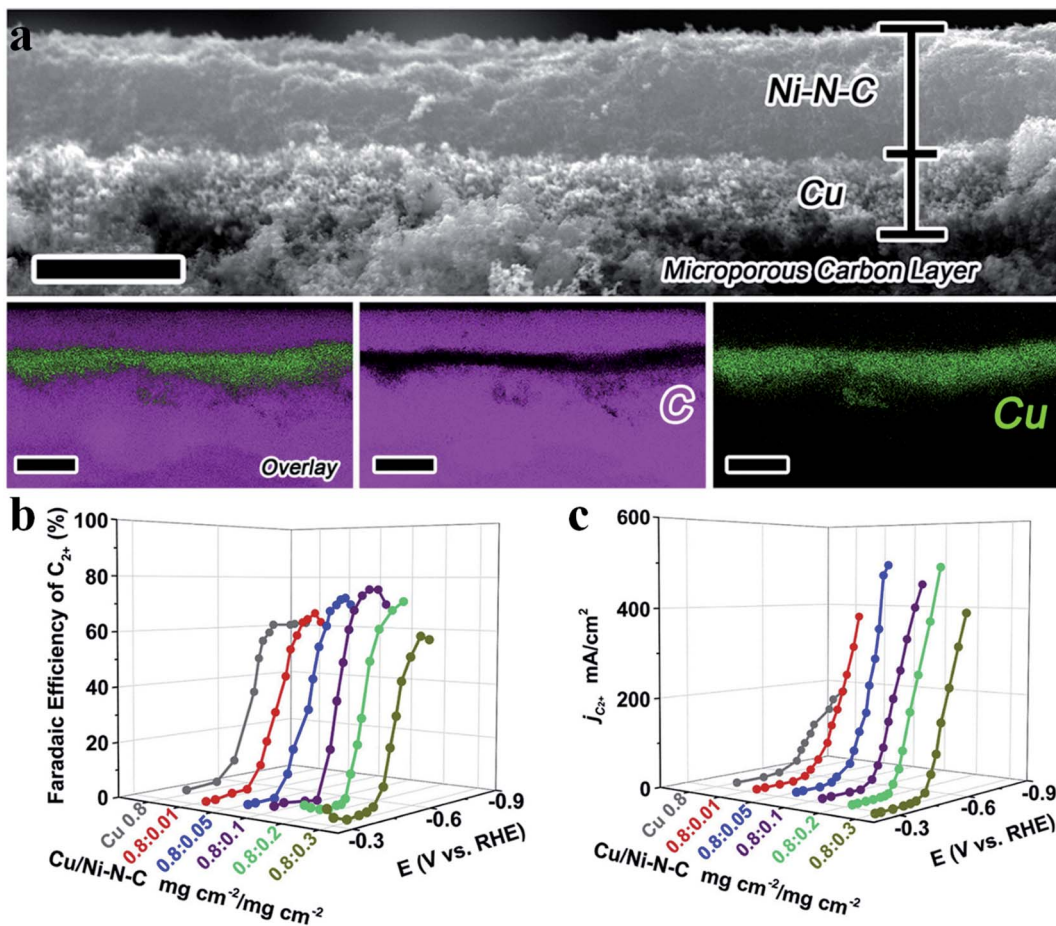


Fig. 13 (a) A cross-sectional SEM image and EDS elemental mapping of a Cu/Ni-N-C tandem electrode with two catalyst layers. Scale bars: 4 μ m for the SEM image and 5 μ m for the elemental mapping. (b) FE $_{C_2^+}$ for the Cu/Ni-N-C tandem electrode with Ni-N-C loading varying from 0.01 to 0.3 mg cm^{-2} . (c) Partial current density of the Cu/Ni-N-C tandem electrode with Ni-N-C loading varying from 0.01 to 0.3 mg cm^{-2} . Reproduced with permission from ref. 115. Copyright (2020) Elsevier.

nanoparticles, which enabled them to reduce CO_2 to CO with a FE of 95.7% at -0.85 V vs. RHE.¹¹⁹ Sun *et al.* reported that Sn single atoms supported on oxygen-deficient CuO could reduce CO_2 to ethylene with a FE of 48.5%, resulting from the lowered CO dimerization energy due to Sn doping.¹²⁰ The CO_2 RR is

Table 1 Products beyond CO using SACs in the CO_2 RR

SACs	Structures	Products	Ref.
$\text{Sn}^{\delta+}$	SnN_2C_2	HCOOH	99
Sb SA/NC	SbN_4	HCOOH	101
NiSn-APC	$\text{N}_4\text{-Ni-Sn-N}_4$	HCOOH	100
Mo-NG	MoN_4	HCOOH	102
CoPc/CNT	CoN_4	CH_3OH	103
CuSA/TCNFs	CuN_4	CH_3OH	105
SA-Zn/MNC	ZnN_4	CH_4	106
CoPc@Zn-N-C	ZnN_4	CH_4	116
Cu-CeO_2	Cu-O_3	CH_4	107
$\text{Cu}_{0.5}\text{NC}$	CuN_4	$\text{C}_2\text{H}_5\text{OH}$	108
Cu/C-0.4	CuO_4	$\text{C}_2\text{H}_5\text{OH}$	109
Cu-N-C-800(900)	$\text{Cu-N}_2(\text{N}_4)$	$\text{C}_2\text{H}_4\&\text{CH}_4$	111
Cu-SA/NPC	CuN_4	CH_3COCH_3	110

limited by the scaling relationship. Hybridizing d-orbitals of transition metals with p-orbitals of main group elements or metal carbides or nitrides offers a promising strategy to break the scaling relationship. Jung *et al.* inserted a series of single metal atoms into the surface defect sites of TiC, denoted as $\text{M}@d\text{-TiC}$,⁴⁹ and Ir@d-TiC was found to display a very low overpotential of only -0.09 V to reduce CO_2 to produce CH_4 . pDOS revealed that the lack of sigma-type bonding interaction between $^*\text{CO}$ and single Ir atoms in Ir@d-TiC resulted in an appreciable decrease in the limiting potential. Inspired by these studies, substrates beyond carbon deserve more attention to be studied.

4. Summary and outlook

To sum up, in this review, we introduced the theoretical considerations to guide the design of CO_2 RR catalysts in terms of HER suppression, generation of C_1 products and formation of C_2^+ products, which were later supported by experiments (Table 1 summarizes the products beyond CO using SACs in the CO_2 RR). Although much progress has been made in this field,

many challenges still remain. In the following we list the main issues and offer our solutions to address these obstacles.

(1) Most of the SACs are prepared at high temperatures ($>800^{\circ}\text{C}$), which makes the synthesis uncontrollable.^{121–123} As a result, the construction of SACs with a precise coordination environment is difficult to realize. Up to now, the coordination number is solely determined by EXAFS. However, EXAFS can only give the average structure^{124–126} of SACs instead of the local structure. The high similarity of the M–C, M–N, and M–O bonds makes it hard to exactly figure out the coordination structure and the coordination number. Also, even if SACs possess the same coordination number, many possible models exist. For example, for the M-SAC with a coordination number of 3, the structure can be M–N₃, M–N₃–C, or M–N₃–V. Moreover, these species can be located in plane or at the edges. The above uncertainty leads to the divergence in the effect of coordination number. Without a definite structure, it is impossible for DFT calculation to simulate the reaction mechanism.^{127–130} Preparing SACs at low temperature or designing immobilized molecular catalysts is able to ensure a well-defined structure.^{131–135} Additionally, more advanced characterization techniques are needed to be developed to better study the structure of SACs.^{136–139}

(2) The structure of SAC does not always remain constant during the electrochemical reaction. For example, Cu single atoms could be transformed into Cu clusters during the CO₂RR. Whether SACs undergo structural transitions and identification of the actual active site(s) in SACs are still the conundrums. *In situ* characterization provides a platform to monitor the structural evolution of SACs during the reaction.^{140–144} Time-resolved *in situ* measurements should be developed to figure out the true active sites and obtain an overall picture of the reaction mechanism.

(3) Multiple protonation and electron transfer steps are involved in the CO₂RR, making the reaction mechanism very complicated.^{145–148} For the C₂₊ products, lots of possible pathways for C–C coupling are proposed but cannot be confirmed by the current characterization techniques.¹⁴⁹ Also, the

distribution of C₂₊ products is broad, and the selectivity is rather poor. Furthermore, it is still unclear whether protonation and electron transfer happen simultaneously (PCET mechanism).^{150–154} Without a thorough understanding of the reaction mechanism, designing and searching for highly active and selective catalysts would be challenging. Constructing SACs with a well-defined structure and coupling *in situ* techniques together with the rapid developing computational methods are conducive to elucidating the underlying reaction mechanisms^{155,156} (Fig. 14).

(4) Most of the SACs are in the form of powder, and show unsatisfactory performance in real devices.^{157–161} Particularly, the solubility of CO₂ is low in aqueous solution (34 mM) and the CO₂ mass diffusion limitation dominates the CO₂RR particularly at high current densities. Hybridizing SACs with a gas diffusion support or designing monolithic SAC electrodes has the potential to tackle this challenge. Moreover, flow cells and membrane electrode assembly cells have been developed rapidly, which assists in further improving CO₂RR performance to meet the industry requirement.^{162–167}

Author contributions

J. Z., H. B. Y., and B. L. conceived the topic and structure of the article. All authors reviewed and contributed to this paper.

Conflicts of interest

There are no conflicts to declare.

Acknowledgements

This work was supported by the fund from the Singapore Ministry of Education Academic Research Fund (AcRF) Tier 1: RG4/20, Tier 2: MOET2EP10120-0002, Agency for Science, Technology and Research (A*Star) IRG: A20E5c0080, Jiangsu Specially-Appointed Professor Program, Interdisciplinary Project of Yangzhou University (yzuxk202013) and National Natural Science Foundation of China (No. 22075195).

References

- 1 Z. Song, L. Zhang, K. Doyle-Davis, X. Fu, J. L. Luo and X. Sun, *Adv. Energy Mater.*, 2020, **10**, 2001561.
- 2 J. Su, R. Ge, Y. Dong, F. Hao and L. Chen, *J. Mater. Chem. A*, 2018, **6**, 14025–14042.
- 3 F. Zhang, H. Zhang and Z. Liu, *Curr. Opin. Green Sust. Chem.*, 2019, **16**, 77–84.
- 4 Y. Chen, K. Chen, J. Fu, A. Yamaguchi, H. Li, H. Pan, J. Hu, M. Miyauchi and M. Liu, *Nano Mater. Sci.*, 2020, **2**, 235–247.
- 5 S. Piontek, K. Junge Puring, D. Siegmund, M. Smialkowski, I. Sinev, D. Tetzlaff, B. R. Cuenya and U.-P. Apfel, *Chem. Sci.*, 2019, **10**, 1075–1081.
- 6 Z. Chen, X. Zhang, M. Jiao, K. Mou, X. Zhang and L. Liu, *Adv. Energy Mater.*, 2020, **10**, 1903664.
- 7 S. Back, J. Lim, N. Y. Kim, Y. H. Kim and Y. Jung, *Chem. Sci.*, 2017, **8**, 1090–1096.

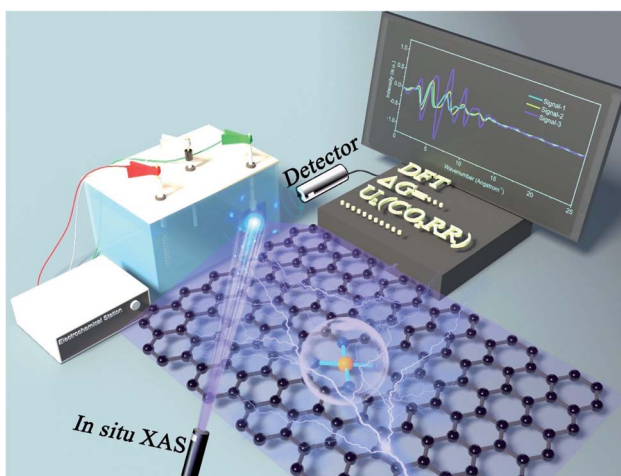


Fig. 14 *In situ* measurements and theoretical calculations prompt the development of SACs.



8 S. Mou, T. Wu, J. Xie, Y. Zhang, L. Ji, H. Huang, T. Wang, Y. Luo, X. Xiong and B. Tang, *Adv. Mater.*, 2019, **31**, 1903499.

9 Q. Gong, P. Ding, M. Xu, X. Zhu, M. Wang, J. Deng, Q. Ma, N. Han, Y. Zhu and J. Lu, *Nat. Commun.*, 2019, **10**, 1–10.

10 J. Kim, W. Choi, J. W. Park, C. Kim, M. Kim and H. Song, *J. Am. Chem. Soc.*, 2019, **141**, 6986–6994.

11 J. Y. Choi, C. K. Lim, B. Park, M. Kim, A. Jamal and H. Song, *J. Mater. Chem. A*, 2019, **7**, 15068–15072.

12 P. Deng, H. Wang, R. Qi, J. Zhu, S. Chen, F. Yang, L. Zhou, K. Qi, H. Liu and B. Y. Xia, *ACS Catal.*, 2019, **10**, 743–750.

13 L. R. L. Ting, R. García-Muelas, A. J. Martín, F. L. Veenstra, S. T. J. Chen, Y. Peng, E. Y. X. Per, S. Pablo-García, N. López and J. Pérez-Ramírez, *Angew. Chem.*, 2020, **132**, 21258–21265.

14 R. Matheu, E. Gutierrez-Puebla, M. Á. Monge, C. S. Diercks, J. Kang, M. S. Prévot, X. Pei, N. Hanikel, B. Zhang and P. Yang, *J. Am. Chem. Soc.*, 2019, **141**, 17081–17085.

15 H. Zhang, X. Chang, J. G. Chen, W. A. Goddard, B. Xu, M.-J. Cheng and Q. Lu, *Nat. Commun.*, 2019, **10**, 1–9.

16 C. Kim, F. Dionigi, V. Beermann, X. Wang, T. Möller and P. Strasser, *Adv. Mater.*, 2019, **31**, 1805617.

17 N. Martić, C. Reller, C. Macauley, M. Löffler, B. Schmid, D. Reinisch, E. Volkova, A. Maltenberger, A. Rucki and K. J. Mayrhofer, *Adv. Energy Mater.*, 2019, **9**, 1901228.

18 N. Wanninayake, Q. Ai, R. Zhou, M. A. Hoque, S. Herrell, M. I. Guzman, C. Risko and D. Y. Kim, *Carbon*, 2020, **157**, 408–419.

19 B. Qiao, A. Wang, X. Yang, L. F. Allard, Z. Jiang, Y. Cui, J. Liu, J. Li and T. Zhang, *Nat. Chem.*, 2011, **3**, 634–641.

20 L. Wang, W. Zhang, S. Wang, Z. Gao, Z. Luo, X. Wang, R. Zeng, A. Li, H. Li and M. Wang, *Nat. Commun.*, 2016, **7**, 1–8.

21 X.-F. Yang, A. Wang, B. Qiao, J. Li, J. Liu and T. Zhang, *Acc. Chem. Res.*, 2013, **46**, 1740–1748.

22 G. X. Pei, X. Y. Liu, X. Yang, L. Zhang, A. Wang, L. Li, H. Wang, X. Wang and T. Zhang, *ACS Catal.*, 2017, **7**, 1491–1500.

23 C. Zhu, S. Fu, J. Song, Q. Shi, D. Su, M. H. Engelhard, X. Li, D. Xiao, D. Li and L. Estevez, *Small*, 2017, **13**, 1603407.

24 L. Jiao, H. Yan, Y. Wu, W. Gu, C. Zhu, D. Du and Y. Lin, *Angew. Chem.*, 2020, **132**, 2585–2596.

25 B. Han, R. Lang, B. Qiao, A. Wang and T. Zhang, *Chin. J. Catal.*, 2017, **38**, 1498–1507.

26 H. Zhang, G. Liu, L. Shi and J. Ye, *Adv. Energy Mater.*, 2018, **8**, 1701343.

27 X. Su, X.-F. Yang, Y. Huang, B. Liu and T. Zhang, *Acc. Chem. Res.*, 2018, **52**, 656–664.

28 X. Li, X. Yang, J. Zhang, Y. Huang and B. Liu, *ACS Catal.*, 2019, **9**, 2521–2531.

29 X. Li, H. Y. Wang, H. Yang, W. Cai, S. Liu and B. Liu, *Small Methods*, 2018, **2**, 1700395.

30 F. Lü, H. Bao, Y. Mi, Y. Liu, J. Sun, X. Peng, Y. Qiu, L. Zhuo, X. Liu and J. Luo, *Sustainable Energy Fuels*, 2020, **4**, 1012–1028.

31 J. Lin, A. Wang, B. Qiao, X. Liu, X. Yang, X. Wang, J. Liang, J. Li, J. Liu and T. Zhang, *J. Am. Chem. Soc.*, 2013, **135**, 15314–15317.

32 B. Zhang, H. Asakura, J. Zhang, J. Zhang, S. De and N. Yan, *Angew. Chem.*, 2016, **128**, 8459–8463.

33 F. Yang, P. Song, X. Liu, B. Mei, W. Xing, Z. Jiang, L. Gu and W. Xu, *Angew. Chem., Int. Ed.*, 2018, **57**, 12303–12307.

34 J. M. Bockris and E. Potter, *J. Electrochem. Soc.*, 1952, **99**, 169.

35 P. C. Vesborg, B. Seger and I. Chorkendorff, *J. Phys. Chem. Lett.*, 2015, **6**, 951–957.

36 Y. Zheng, Y. Jiao, M. Jaroniec and S. Z. Qiao, *Angew. Chem., Int. Ed.*, 2015, **54**, 52–65.

37 X. Shen, X. Liu, S. Wang, T. Chen, W. Zhang, L. Cao, T. Ding, Y. Lin, D. Liu, L. Wang, W. Zhang and T. Yao, *Nano Lett.*, 2021, **21**, 686–692.

38 T. Zhang, X. Han, H. Yang, A. Han, E. Hu, Y. Li, X. Q. Yang, L. Wang, J. Liu and B. Liu, *Angew. Chem., Int. Ed.*, 2020, **59**, 12055–12061.

39 W. Ren, X. Tan, W. Yang, C. Jia, S. Xu, K. Wang, S. C. Smith and C. Zhao, *Angew. Chem., Int. Ed.*, 2019, **58**, 6972–6976.

40 R. M. Enick and S. M. Klara, *Chem. Eng. Commun.*, 1990, **90**, 23–33.

41 P. Singh, D. W. Brilman and M. J. Groeneveld, *Int. J. Greenhouse Gas Control*, 2011, **5**, 61–68.

42 L. W. Diamond and N. N. Akinfiev, *Fluid Phase Equilib.*, 2003, **208**, 265–290.

43 D. M. Weekes, D. A. Salvatore, A. Reyes, A. Huang and C. P. Berlinguette, *Acc. Chem. Res.*, 2018, **51**, 910–918.

44 S. Yao, S. Hosohara, Y. Shimizu, N. Miura, H. Futata and N. Yamazoe, *Chem. Lett.*, 1991, **20**, 2069–2072.

45 S. Zhang, Q. Fan, R. Xia and T. J. Meyer, *Acc. Chem. Res.*, 2020, **53**, 255–264.

46 W.-H. Wang, Y. Himeda, J. T. Muckerman, G. F. Manbeck and E. Fujita, *Chem. Rev.*, 2015, **115**, 12936–12973.

47 Y. Hori, K. Kikuchi and S. Suzuki, *Chem. Lett.*, 1985, **14**, 1695–1698.

48 W. Li, M. Seredych, E. Rodríguez-Castellón and T. J. Bandosz, *ChemSusChem*, 2016, **9**, 606–616.

49 S. Back and Y. Jung, *ACS Energy Lett.*, 2017, **2**, 969–975.

50 C. Ao, B. Feng, S. Qian, L. Wang, W. Zhao, Y. Zhai and L. Zhang, *J. CO₂ Util.*, 2020, **36**, 116–123.

51 D. Y. Shin, J. S. Won, J. A. Kwon, M.-S. Kim and D.-H. Lim, *Comput. Theor. Chem.*, 2017, **1120**, 84–90.

52 M. Le, M. Ren, Z. Zhang, P. T. Sprunger, R. L. Kurtz and J. C. Flake, *J. Electrochem. Soc.*, 2011, **158**, E45.

53 Y. Kotb, S.-E. K. Fateen, J. Albo and I. Ismail, *J. Electrochem. Soc.*, 2017, **164**, E391.

54 M. Tang, H. Shen, H. Xie and Q. Sun, *ChemPhysChem*, 2020, **21**, 779–784.

55 L. Ji, L. Li, X. Ji, Y. Zhang, S. Mou, T. Wu, Q. Liu, B. Li, X. Zhu and Y. Luo, *Angew. Chem.*, 2020, **132**, 768–772.

56 E. Boutin, M. Wang, J. C. Lin, M. Mesnage, D. Mendoza, B. Lassalle-Kaiser, C. Hahn, T. F. Jaramillo and M. Robert, *Angew. Chem., Int. Ed.*, 2019, **58**, 16172–16176.

57 D. Ren, Y. Deng, A. D. Handoko, C. S. Chen, S. Malkhandi and B. S. Yeo, *ACS Catal.*, 2015, **5**, 2814–2821.

58 S. Kusama, T. Saito, H. Hashiba, A. Sakai and S. Yotsuhashi, *ACS Catal.*, 2017, **7**, 8382–8385.



59 N. Altaf, S. Liang, R. Iqbal, M. Hayat, T. R. Reina and Q. Wang, *J. CO₂ Util.*, 2020, **40**, 101205.

60 H. Ning, X. Wang, W. Wang, Q. Mao, Z. Yang, Q. Zhao, Y. Song and M. Wu, *Carbon*, 2019, **146**, 218–223.

61 Y. Hori, A. Murata, R. Takahashi and S. Suzuki, *Chem. Commun.*, 1988, 17–19.

62 D. W. DeWulf, T. Jin and A. J. Bard, *J. Electrochem. Soc.*, 1989, **136**, 1686.

63 C. Genovese, M. E. Schuster, E. K. Gibson, D. Gianolio, V. Posligha, R. Grau-Crespo, G. Cibin, P. P. Wells, D. Garai and V. Solokha, *Nat. Commun.*, 2018, **9**, 1–12.

64 R. De, S. Gonglach, S. Paul, M. Haas, S. Sreejith, P. Gerschel, U. P. Apfel, T. H. Vuong, J. Rabeah and S. Roy, *Angew. Chem.*, 2020, **132**, 10614–10621.

65 G. Feng, W. Chen, B. Wang, Y. Song, G. Li, J. Fang, W. Wei and Y. Sun, *Chem.-Asian J.*, 2018, **13**, 1992–2008.

66 C. Chen, J. F. K. Kotyk and S. W. Sheehan, *Chem.*, 2018, **4**, 2571–2586.

67 L. Jiao, W. Yang, G. Wan, R. Zhang, X. Zheng, H. Zhou, S. H. Yu and H. L. Jiang, *Angew. Chem., Int. Ed.*, 2020, **59**, 20589–20595.

68 W. Ju, A. Bagger, G. P. Hao, A. S. Varela, I. Sinev, V. Bon, B. Roldan Cuenya, S. Kaskel, J. Rossmeisl and P. Strasser, *Nat. Commun.*, 2017, **8**, 944.

69 H. Yang, Q. Lin, C. Zhang, X. Yu, Z. Cheng, G. Li, Q. Hu, X. Ren, Q. Zhang and J. Liu, *Nat. Commun.*, 2020, **11**, 1–8.

70 S. Liu, H. B. Yang, S. F. Hung, J. Ding, W. Cai, L. Liu, J. Gao, X. Li, X. Ren and Z. Kuang, *Angew. Chem., Int. Ed.*, 2020, **59**, 798–803.

71 Q. He, D. Liu, J. H. Lee, Y. Liu, Z. Xie, S. Hwang, S. Kattel, L. Song and J. G. Chen, *Angew. Chem., Int. Ed.*, 2020, **59**, 3033–3037.

72 Y. Cheng, S. Zhao, B. Johannessen, J. P. Veder, M. Saunders, M. R. Rowles, M. Cheng, C. Liu, M. F. Chisholm and R. De Marco, *Adv. Mater.*, 2018, **30**, 1706287.

73 P. Lu, Y. Yang, J. Yao, M. Wang, S. Dipazir, M. Yuan, J. Zhang, X. Wang, Z. Xie and G. Zhang, *Appl. Catal., B*, 2019, **241**, 113–119.

74 X. Wang, Z. Chen, X. Zhao, T. Yao, W. Chen, R. You, C. Zhao, G. Wu, J. Wang, W. Huang, J. Yang, X. Hong, S. Wei, Y. Wu and Y. Li, *Angew. Chem., Int. Ed.*, 2018, **57**, 1944–1948.

75 L. Zhang, J. Xiao, H. Wang and M. Shao, *ACS Catal.*, 2017, **7**, 7855–7865.

76 C. Zhao, Y. Wang, Z. Li, W. Chen, Q. Xu, D. He, D. Xi, Q. Zhang, T. Yuan, Y. Qu, J. Yang, F. Zhou, Z. Yang, X. Wang, J. Wang, J. Luo, Y. Li, H. Duan, Y. Wu and Y. Li, *Joule*, 2019, **3**, 584–594.

77 J. Feng, H. Gao, L. Zheng, Z. Chen, S. Zeng, C. Jiang, H. Dong, L. Liu, S. Zhang and X. Zhang, *Nat. Commun.*, 2020, **11**, 4341.

78 J. Zhang, H. Yang and B. Liu, *Adv. Energy Mater.*, 2021, **11**, 2002473.

79 G. Gao, S. Bottle and A. Du, *Catal. Sci. Technol.*, 2018, **8**, 996–1001.

80 H. Xu, D. Cheng, D. Cao and X. C. Zeng, *Nat. Catal.*, 2018, **1**, 339–348.

81 Y. Wang, G. Jia, X. Cui, X. Zhao, Q. Zhang, L. Gu, L. Zheng, L.-H. Li, Q. Wu and D. J. Singh, *Chem.*, 2021, **7**, 436–449.

82 X. Li, H. Rong, J. Zhang, D. Wang and Y. Li, *Nano Res.*, 2020, **13**, 1842–1855.

83 Y. Lin, P. Liu, E. Velasco, G. Yao, Z. Tian, L. Zhang and L. Chen, *Adv. Mater.*, 2019, **31**, 1808193.

84 J. Gu, C.-S. Hsu, L. Bai, H. M. Chen and X. Hu, *Science*, 2019, **364**, 1091–1094.

85 H. Zhang, J. Wei, J. Dong, G. Liu, L. Shi, P. An, G. Zhao, J. Kong, X. Wang and X. Meng, *Angew. Chem.*, 2016, **128**, 14522–14526.

86 D. Yang, H. Yu, T. He, S. Zuo, X. Liu, H. Yang, B. Ni, H. Li, L. Gu and D. Wang, *Nat. Commun.*, 2019, **10**, 1–10.

87 L. Sun, Z. Huang, V. Reddu, T. Su, A. C. Fisher and X. Wang, *Angew. Chem., Int. Ed.*, 2020, **59**, 17104–17109.

88 K. Jiang, S. Siahrostami, T. Zheng, Y. Hu, S. Hwang, E. Stavitski, Y. Peng, J. Dynes, M. Gangisetty and D. Su, *Energy Environ. Sci.*, 2018, **11**, 893–903.

89 J. Liu, X. Kong, L. Zheng, X. Guo, X. Liu and J. Shui, *ACS Nano*, 2020, **14**, 1093–1101.

90 N. Wang, Z. Liu, J. Ma, J. Liu, P. Zhou, Y. Chao, C. Ma, X. Bo, J. Liu and Y. Hei, *ACS Sustainable Chem. Eng.*, 2020, **8**, 13813–13822.

91 Y. Cheng, S. Yang, S. P. Jiang and S. Wang, *Small Methods*, 2019, **3**, 1800440.

92 H. B. Yang, S.-F. Hung, S. Liu, K. Yuan, S. Miao, L. Zhang, X. Huang, H.-Y. Wang, W. Cai and R. Chen, *Nat. Energy*, 2018, **3**, 140–147.

93 B. Zhang, J. Zhang, J. Shi, D. Tan, L. Liu, F. Zhang, C. Lu, Z. Su, X. Tan and X. Cheng, *Nat. Commun.*, 2019, **10**, 1–8.

94 W. Zhu, L. Zhang, S. Liu, A. Li, X. Yuan, C. Hu, G. Zhang, W. Deng, K. Zang, J. Luo, Y. Zhu, M. Gu, Z. J. Zhao and J. Gong, *Angew. Chem., Int. Ed.*, 2020, **59**, 12664–12668.

95 W. Ren, X. Tan, W. Yang, C. Jia, S. Xu, K. Wang, S. C. Smith and C. Zhao, *Angew. Chem., Int. Ed.*, 2019, **58**, 6972–6976.

96 X. Ren, S. Liu, H. Li, J. Ding, L. Liu, Z. Kuang, L. Li, H. Yang, F. Bai, Y. Huang, T. Zhang and B. Liu, *Sci. China: Chem.*, 2020, **63**, 1727–1733.

97 X. Zhang, Z. Wu, X. Zhang, L. Li, Y. Li, H. Xu, X. Li, X. Yu, Z. Zhang, Y. Liang and H. Wang, *Nat. Commun.*, 2017, **8**, 14675.

98 M. Wang, K. Torbensen, D. Salvatore, S. Ren, D. Joulié, F. Dumoulin, D. Mendoza, B. Lassalle-Kaiser, U. Işçi and C. P. Berlinguette, *Nat. Commun.*, 2019, **10**, 1–8.

99 X. Zu, X. Li, W. Liu, Y. Sun, J. Xu, T. Yao, W. Yan, S. Gao, C. Wang, S. Wei and Y. Xie, *Adv. Mater.*, 2019, **31**, e1808135.

100 W. Xie, H. Li, G. Cui, J. Li, Y. Song, S. Li, X. Zhang, J. Y. Lee, M. Shao and M. Wei, *Angew. Chem., Int. Ed.*, 2020, **60**, 7382–7388.

101 Z. Jiang, T. Wang, J. Pei, H. Shang, D. Zhou, H. Li, J. Dong, Y. Wang, R. Cao, Z. Zhuang, W. Chen, D. Wang, J. Zhang and Y. Li, *Energy Environ. Sci.*, 2020, **13**, 2856–2863.

102 P. Huang, M. Cheng, H. Zhang, M. Zuo, C. Xiao and Y. Xie, *Nano Energy*, 2019, **61**, 428–434.

103 Y. Wu, Z. Jiang, X. Lu, Y. Liang and H. Wang, *Nature*, 2019, **575**, 639–642.



104 Z. Wang, J. Zhao and Q. Cai, *Phys. Chem. Chem. Phys.*, 2017, **19**, 23113–23121.

105 H. Yang, Y. Wu, G. Li, Q. Lin, Q. Hu, Q. Zhang, J. Liu and C. He, *J. Am. Chem. Soc.*, 2019, **141**, 12717–12723.

106 L. Han, S. Song, M. Liu, S. Yao, Z. Liang, H. Cheng, Z. Ren, W. Liu, R. Lin, G. Qi, X. Liu, Q. Wu, J. Luo and H. L. Xin, *J. Am. Chem. Soc.*, 2020, **142**, 12563–12567.

107 Y. Wang, Z. Chen, P. Han, Y. Du, Z. Gu, X. Xu and G. Zheng, *ACS Catal.*, 2018, **8**, 7113–7119.

108 D. Karapinar, N. T. Huan, N. Ranjbar Sahraie, J. Li, D. Wakerley, N. Touati, S. Zanna, D. Taverna, L. H. Galvao Tizei, A. Zitolo, F. Jaouen, V. Mougel and M. Fontecave, *Angew. Chem., Int. Ed.*, 2019, **58**, 15098–15103.

109 H. Xu, D. Rebollar, H. He, L. Chong, Y. Liu, C. Liu, C.-J. Sun, T. Li, J. V. Muntean, R. E. Winans, D.-J. Liu and T. Xu, *Nat. Energy*, 2020, **5**, 623–632.

110 K. Zhao, X. Nie, H. Wang, S. Chen, X. Quan, H. Yu, W. Choi, G. Zhang, B. Kim and J. G. Chen, *Nat. Commun.*, 2020, **11**, 2455.

111 A. Guan, Z. Chen, Y. Quan, C. Peng, Z. Wang, T.-K. Sham, C. Yang, Y. Ji, L. Qian, X. Xu and G. Zheng, *ACS Energy Lett.*, 2020, **5**, 1044–1053.

112 Y. Jiao, Y. Zheng, P. Chen, M. Jaroniec and S. Z. Qiao, *J. Am. Chem. Soc.*, 2017, **139**, 18093–18100.

113 J. Gao, H. Zhang, X. Guo, J. Luo, S. M. Zakeeruddin, D. Ren and M. Grätzel, *J. Am. Chem. Soc.*, 2019, **141**, 18704–18714.

114 X. Wang, J. F. de Araújo, W. Ju, A. Bagger, H. Schmies, S. Kühl, J. Rossmeisl and P. Strasser, *Nat. Nanotechnol.*, 2019, **14**, 1063–1070.

115 X. She, T. Zhang, Z. Li, H. Li, H. Xu and J. Wu, *Cell Rep. Phys. Sci.*, 2020, **1**, 100051.

116 L. Lin, T. Liu, J. Xiao, H. Li, P. Wei, D. Gao, B. Nan, R. Si, G. Wang and X. Bao, *Angew. Chem., Int. Ed.*, 2020, **59**, 22408–22413.

117 T. Zhang, A. G. Walsh, J. Yu and P. Zhang, *Chem. Soc. Rev.*, 2021, **50**, 569–588.

118 R. T. Hannagan, G. Giannakakis, M. Flytzani-Stephanopoulos and E. C. H. Sykes, *Chem. Rev.*, 2020, **120**, 12044–12088.

119 N. Zhang, X. Zhang, L. Tao, P. Jiang, C. Ye, R. Lin, Z. Huang, A. Li, D. Pang and H. Yan, *Angew. Chem., Int. Ed.*, 2021, **60**, 6170–6176.

120 Y. Jiang, C. Choi, S. Hong, S. Chu, T.-S. Wu, Y.-L. Soo, L. Hao, Y. Jung and Z. Sun, *Cell Rep. Phys. Sci.*, 2021, **2**, 100356.

121 H. Fei, J. Dong, Y. Feng, C. S. Allen, C. Wan, B. Volosovskiy, M. Li, Z. Zhao, Y. Wang and H. Sun, *Nat. Catal.*, 2018, **1**, 63–72.

122 M. Xiao, J. Zhu, L. Ma, Z. Jin, J. Ge, X. Deng, Y. Hou, Q. He, J. Li and Q. Jia, *ACS Catal.*, 2018, **8**, 2824–2832.

123 H. Yang, L. Shang, Q. Zhang, R. Shi, G. I. Waterhouse, L. Gu and T. Zhang, *Nat. Commun.*, 2019, **10**, 1–9.

124 F. De Groot, *Chem. Rev.*, 2001, **101**, 1779–1808.

125 J. Yano and V. K. Yachandra, *Photosynth. Res.*, 2009, **102**, 241.

126 D. Koningsberger and R. Prins, *X-ray absorption: principles, applications, techniques of EXAFS, SEXAFS, and XANES*, 1988.

127 Y. Gao, Z. Cai, X. Wu, Z. Lv, P. Wu and C. Cai, *ACS Catal.*, 2018, **8**, 10364–10374.

128 Z. Lu, P. Lv, Y. Liang, D. Ma, Y. Zhang, W. Zhang, X. Yang and Z. Yang, *Phys. Chem. Chem. Phys.*, 2016, **18**, 21865–21870.

129 Y. Feng, Q. Wan, H. Xiong, S. Zhou, X. Chen, X. I. Pereira Hernandez, Y. Wang, S. Lin, A. K. Datye and H. Guo, *J. Phys. Chem. C*, 2018, **122**, 22460–22468.

130 L. Qin, Y. Q. Cui, T. L. Deng, F. H. Wei and X. F. Zhang, *ChemPhysChem*, 2018, **19**, 3346–3349.

131 R. Brimblecombe, A. Koo, G. C. Dismukes, G. F. Swiegers and L. Spiccia, *J. Am. Chem. Soc.*, 2010, **132**, 2892–2894.

132 F. Li, B. Zhang, X. Li, Y. Jiang, L. Chen, Y. Li and L. Sun, *Angew. Chem.*, 2011, **123**, 12484–12487.

133 S. W. Sheehan, J. M. Thomsen, U. Hintermair, R. H. Crabtree, G. W. Brudvig and C. A. Schmuttenmaer, *Nat. Commun.*, 2015, **6**, 1–9.

134 P. Garrido-Barros, C. Gimbert-Suriñach, R. Matheu, X. Sala and A. Llobet, *Chem. Soc. Rev.*, 2017, **46**, 6088–6098.

135 B. C. Martindale, G. A. Hutton, C. A. Caputo and E. Reisner, *J. Am. Chem. Soc.*, 2015, **137**, 6018–6025.

136 J. Liu, B. R. Bunes, L. Zang and C. Wang, *Environ. Chem. Lett.*, 2018, **16**, 477–505.

137 A. Vasileff, Y. Zhu, X. Zhi, Y. Zhao, L. Ge, H. M. Chen, Y. Zheng and S. Z. Qiao, *Angew. Chem.*, 2020, **59**, 19649–19653.

138 C. Xu, A. Vasileff, Y. Zheng and S. Z. Qiao, *Adv. Mater. Interfaces*, 2021, **8**, 2001904.

139 C. Xu, X. Zhi, A. Vasileff, D. Wang, B. Jin, Y. Jiao, Y. Zheng and S.-Z. Qiao, *Small Structures*, 2021, **2**, 2000058.

140 S. Mukerjee, T. Thurston, N. Jisrawi, X. Yang, J. McBreen, M. Daroux and X. Xing, *J. Electrochem. Soc.*, 1998, **145**, 466.

141 S. Cheong, J. Watt, B. Ingham, M. F. Toney and R. D. Tilley, *J. Am. Chem. Soc.*, 2009, **131**, 14590–14595.

142 F. Hui, C. Li, Y. Chen, C. Wang, J. Huang, A. Li, W. Li, J. Zou and X. Han, *Nano Res.*, 2020, **13**, 3019–3024.

143 W. Yang, Y. Kim, P. K. Liu, M. Sahimi and T. T. Tsotsis, *Chem. Eng. Sci.*, 2002, **57**, 2945–2953.

144 K. Rhodes, R. Meisner, Y. Kim, N. Dudney and C. Daniel, *J. Electrochem. Soc.*, 2011, **158**, A890.

145 M. Asadi, B. Kumar, A. Behranginia, B. A. Rosen, A. Baskin, N. Repnin, D. Pisasale, P. Phillips, W. Zhu and R. Haasch, *Nat. Commun.*, 2014, **5**, 1–8.

146 X. Liu, J. Xiao, H. Peng, X. Hong, K. Chan and J. K. Nørskov, *Nat. Commun.*, 2017, **8**, 1–7.

147 F. S. Roberts, K. P. Kuhl and A. Nilsson, *Angew. Chem.*, 2015, **127**, 5268–5271.

148 C. Costentin, M. Robert and J.-M. Savéant, *Chem. Soc. Rev.*, 2013, **42**, 2423–2436.

149 Q. Lu, J. Rosen, Y. Zhou, G. S. Hutchings, Y. C. Kimmel, J. G. Chen and F. Jiao, *Nat. Commun.*, 2014, **5**, 1–6.

150 A. D. Handoko, F. Wei, B. S. Yeo and Z. W. Seh, *Nat. Catal.*, 2018, **1**, 922–934.

151 B. Mondal, J. Song, F. Neese and S. Ye, *Curr. Opin. Chem. Biol.*, 2015, **25**, 103–109.



152 L. R. L. Ting and B. S. Yeo, *Curr. Opin. Electrochem.*, 2018, **8**, 126–134.

153 S. Ringe, C. G. Morales-Guio, L. D. Chen, M. Fields, T. F. Jaramillo, C. Hahn and K. Chan, *Nat. Commun.*, 2020, **11**, 1–11.

154 A. Bachmeier and F. Armstrong, *Curr. Opin. Chem. Biol.*, 2015, **25**, 141–151.

155 X. Li, L. Liu, X. Ren, J. Gao, Y. Huang and B. Liu, *Sci. Adv.*, 2020, **6**, eabb6833.

156 Y. Zheng, A. Vasileff, X. Zhou, Y. Jiao, M. Jaroniec and S.-Z. Qiao, *J. Am. Chem. Soc.*, 2019, **141**, 7646–7659.

157 J. Zhang, H. Yang, J. Gao, S. Xi, W. Cai, J. Zhang, P. Cui and B. Liu, *Carbon Energy*, 2020, **2**, 276–282.

158 J. Gao, H. bin Yang, X. Huang, S.-F. Hung, W. Cai, C. Jia, S. Miao, H. M. Chen, X. Yang and Y. Huang, *Chem.*, 2020, **6**, 658–674.

159 J. Gao and B. Liu, *ACS Mater. Lett.*, 2020, **2**, 1008–1024.

160 L. Huang, J. Chen, L. Gan, J. Wang and S. Dong, *Sci. Adv.*, 2019, **5**, eaav5490.

161 S. Liang, C. Hao and Y. Shi, *ChemCatChem*, 2015, **7**, 2559–2567.

162 T. Frey and M. Linardi, *Electrochim. Acta*, 2004, **50**, 99–105.

163 R. H. Barton, P. R. Gibb, J. A. Ronne and H. H. Voss, Membrane Electrode Assembly for an Electrochemical Fuel Cell and a Method of Making an Improved Membrane Electrode Assembly, *US Pat.*, 6057054, 2000.

164 L.-C. Weng, A. T. Bell and A. Z. Weber, *Energy Environ. Sci.*, 2019, **12**, 1950–1968.

165 J. K. Jang, H. S. Moon, I. S. Chang and B. H. Kim, *J. Microbiol. Biotechnol.*, 2005, **15**, 438–441.

166 W. Sun, W. Zhang, H. Su, P. Leung, L. Xing, L. Xu, C. Yang and Q. Xu, *Int. J. Hydrogen Energy*, 2019, **44**, 32231–32239.

167 S.-F. Hung, *Pure Appl. Chem.*, 2020, **92**, 1937–1951.

